

# DSwinIR: Rethinking Window-based Attention for Image Restoration

Gang Wu, *Student Member, IEEE*, Junjun Jiang, *Senior Member, IEEE*, Kui Jiang, *Member, IEEE*, Xianming Liu, *Member, IEEE*, and Liqiang Nie, *Senior Member, IEEE*

**Abstract**—Image restoration has witnessed significant advancements with the development of deep learning models. Transformer-based models, particularly those using window-based self-attention, have become a dominant force. However, their performance is constrained by the rigid, non-overlapping window partitioning scheme, which leads to *insufficient feature interaction across windows and limited receptive fields*. This highlights the need for more adaptive and flexible attention mechanisms. In this paper, we propose the Deformable Sliding Window Transformer for Image Restoration (DSwinIR), a new attention mechanism: the Deformable Sliding Window (DSwin) Attention. This mechanism introduces a token-centric and content-aware paradigm that moves beyond the grid and fixed window partition. It comprises two complementary components. First, it replaces the rigid partitioning with a *token-centric sliding window* paradigm, making it effective at eliminating boundary artifacts. Second, it incorporates a *content-aware deformable sampling* strategy, which allows the attention mechanism to learn data-dependent offsets and actively shape its receptive field to focus on the most informative image regions. Extensive experiments show that DSwinIR achieves strong results, including state-of-the-art performance on several evaluated benchmarks. For instance, in all-in-one image restoration, our DSwinIR surpasses the most recent backbone GridFormer by 0.53 dB on the three-task benchmark and 0.87 dB on the five-task benchmark. The code and pre-trained models are available at <https://github.com/Aitical/DSwinIR>.

**Index Terms**—All-in-One Image Restoration, Image Deraining, Image Dehazing, Image Denoising, Vision Transformer, Deformable Attention

## I. INTRODUCTION

IMAGE restoration aims to recover high-quality images from inputs degraded by noise, rain, haze, blur, low light, and other factors [1]–[5]. Deep learning has led to substantial progress, initially with CNNs [6], [7] and more recently, with Vision Transformers (ViTs) [8] that model long-range dependencies.

The practical use of vanilla Transformers for image restoration is impeded by the quadratic cost of global self-attention with respect to input resolution. Window-based self-attention

The research was supported by the National Natural Science Foundation of China (U23B2009, 62471158) and the Natural Science Foundation of Heilongjiang Province of China for Excellent Youth Project (YQ2024F006).

G. Wu, J. Jiang, K. Jiang, and X. Liu are with the School of Computer Science and Technology, Harbin Institute of Technology, Harbin 150001, China. E-mail: {gww@hit.edu.cn, jiangjunjun@hit.edu.cn, jiangkui@hit.edu.cn, csxm@hit.edu.cn}. Corresponding author: Junjun Jiang.

L. Nie is with the School of Computer Science and Technology, Harbin Institute of Technology (Shenzhen), Shenzhen 518055, China. E-mail: {nieliqiang@gmail.com}.

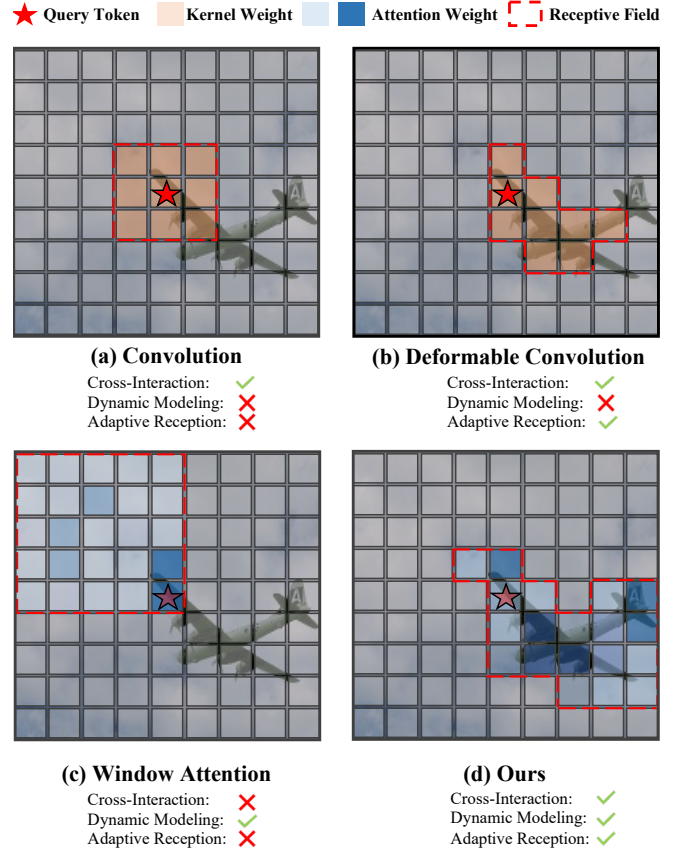


Fig. 1. Comparative analysis of feature extraction mechanisms with an anchor token (marked by ★) as the reference point. (a) Vanilla convolution applies a fixed sampling pattern, leveraging neighborhood features. (b) Deformable convolution introduces adaptive sampling locations based on content, enabling more effective feature integration from relevant regions. (c) Window attention suffers from boundary constraints where anchor tokens near window edges (especially corners) have limited receptive fields. (d) The proposed Deformable Sliding Window (DSwin) attention extends window attention with a token-centric paradigm and the content-aware sampling, bringing robust feature aggregation for anchor tokens.

[9], adopted in SwinIR [10] and Uformer [11], has therefore become the *de facto* choice, striking a favorable trade-off between fidelity and efficiency by restricting computation to local, non-overlapping windows. It introduces two salient limitations: 1) *Boundary Context Truncation*. Consider a token at a window corner: its receptive field is clipped precisely where informative context often lies across the boundary. As a result, its representation collapses toward its nearest in-window neighbors rather than the true cross-window structure it belongs to, producing suboptimal, biased features. 2) *In-*

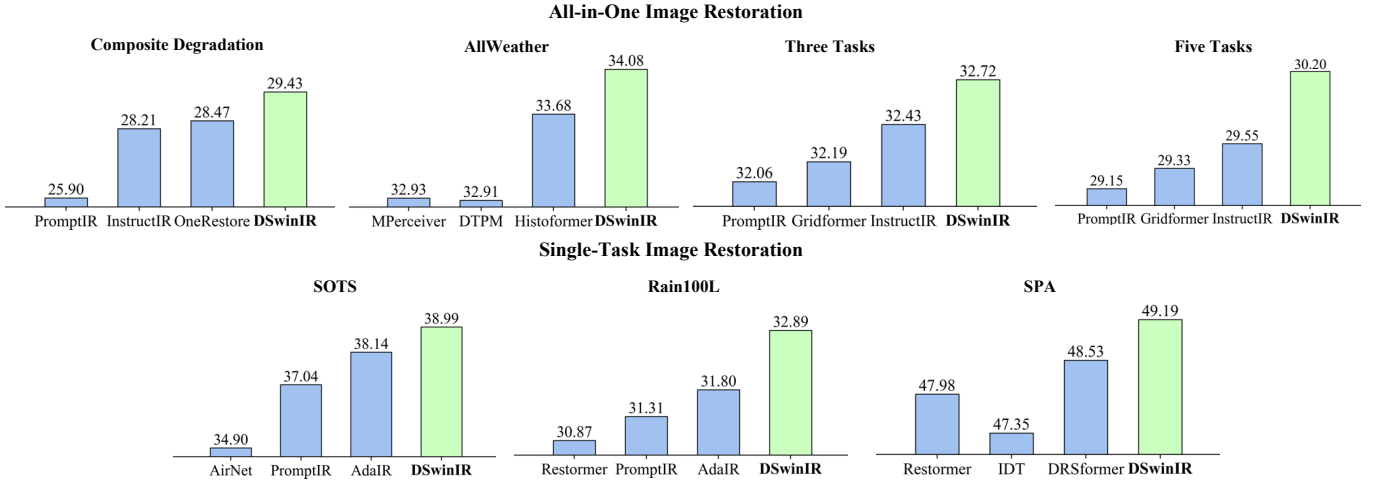


Fig. 2. Quantitative comparison of the proposed DSwinIR against existing methods across diverse image restoration tasks, achieving consistent superior performance. All metrics are reported in PSNR (dB).

*flexible Receptive Fields*: The fixed, square-shaped attention pattern is applied uniformly across the image, failing to adapt to the diverse and anisotropic nature of image content and degradation patterns. Subsequent efforts introduce hand-crafted interaction patterns, such as cross-shaped windows [12], axial stripes [13], and sparse token sampling [14]. While effective, these essentially replace one fixed interaction pattern with another, leaving the core limitation unresolved. They fall short of addressing the core, underlying principle: the shape and scope of an attention field should be dynamically determined by the image content itself, not by a predefined, static template.

In this work, we move beyond such predefined, static patterns and advocate that an effective attention mechanism for image restoration is both *token-centric* and *content-aware*. Motivated by this view, we introduce Deformable Sliding Window (DSwin) Attention, a redesign of windowed attention (Figure 1). First, to strengthen cross-window interaction, we embrace a *token-centric sliding window* paradigm: every token attends within its own centered neighborhood, creating overlaps that reduce boundary effects. Second, to tackle the inflexible receptive field, we introduce a *content-aware deformable mechanism*: learned offsets adapt the sampling pattern to image structure (e.g., diagonal rain streaks or object contours). Building upon core components, we present the Deformable Sliding Window Transformer for Image Restoration (DSwinIR). It integrates the DSwin attention module, offering a flexible and robust backbone for diverse image restoration tasks.

In recent years, the development of all-in-one image restoration models, handling multiple types of degradation within a unified framework, has gained increasing attention [5]. We evaluate DSwinIR in the all-in-one setting. Strengthening the backbone architecture offers an underexplored alternative to prompt-based approaches [15], [16]. Empirically, DSwinIR matches or exceeds several prompt-based methods on our benchmarks. We conduct extensive evaluations across diverse image restoration tasks, spanning both all-in-one multiple

degradation scenarios and specialized single-task settings. As illustrated in Figure 2, DSwinIR delivers substantial improvements across diverse benchmarks.

The main contributions of this work are summarized as follows:

- We propose a novel Deformable Sliding Window (DSwin) Attention mechanism. It adopts a token-centric, content-aware design that addresses boundary truncation and inflexible receptive fields in window-based attention.
- We develop DSwinIR, a new and general backbone architecture for image restoration built upon the DSwin attention module. The architecture cohesively integrates multi-scale feature extraction in both the attention and feed-forward network modules, further enhancing its representation capacity.
- Through extensive experiments on a diverse array of benchmarks, including all-in-one and single-task restoration scenarios, we demonstrate that DSwinIR consistently achieves competitive or superior performance compared to existing methods on the evaluated datasets.

The remainder of this paper is organized as follows. Section II provides a comprehensive review of the image restoration literature. Section III elaborates on our proposed method. Section IV presents extensive experimental validation on a wide array of benchmarks. Finally, Section V concludes the paper by summarizing our key contributions and their broader significance for the field.

## II. RELATED WORK

Image restoration, a classic and long-standing challenge in computer vision, has seen decades of research [17]. It has a wide-ranging impact on various downstream tasks, from enhancing visual data for autonomous driving [18] and improving the robustness of person re-identification [19] to enabling one-click image correction for cellular segmentation in bioinformatics [20]. Nowadays, the advent of deep learning has dramatically accelerated progress in this field [21], leading

to remarkable breakthroughs in specialized tasks like denoising [1], dehazing [2], and deraining [3]. More recently, the field’s focus has evolved from single-task models to highly versatile *all-in-one frameworks* [5], which are more practical for real-world scenarios involving complex, mixed degradations. In this section, we chart this evolution to contextualize our contribution.

### A. Single-Task Image Restoration

Deep learning, particularly with the rise of Convolutional Neural Networks (CNNs), has long been the cornerstone of image restoration. Leveraging a data-driven paradigm, CNNs have proven highly effective compared to classical approaches [17], establishing strong foundations in tasks such as image super-resolution [22], image denoising [6], image deraining [23], and image dehazing [24]. Subsequently, numerous more sophisticated studies emerged, as well as those incorporating residual or dense connections [25], [26], as well as those exploring channel attention [27] and non-local attention mechanisms [28]. Within specific domains, landmark contributions have guided the field; for instance, in image deraining, Jiang *et al.* proposed MSPFN [29], which introduced a progressive learning paradigm that inspired a series of subsequent works [30]–[32]. Image dehazing has also seen many representative studies, such as FFANet [33], and more recent explorations with novel network designs [34], [35]. Similarly, Feijoo *et al.* [36] exploit a light-weight yet powerful model for low-light image enhancement in the proposed DarkIR. In parallel, researchers have also focused on developing general restoration architectures applicable to multiple tasks, including MPRNet [37], NAFNet [38], FSNet [39], IRNeXT [40], ConvIR [41], and MB-TaylorFormer [42]. However, these powerful models still typically require separate training for each individual task.

Concurrently, to better model the complex, non-local dependencies often present in degradations, Vision Transformers (ViTs) [8] have garnered significant attention for their powerful dynamic modeling capabilities. While early models like IPT [43] were computationally intensive, the window-based local attention of the Swin Transformer [9] provided an efficient and effective foundation. This spawned a new generation of influential backbones, including SwinIR [10] and Uformer [11]. These advancements were also channeled into powerful task-specific transformers like IDT [44] for image deraining and Dehazformer [45] for image dehazing. A significant thread of subsequent research has focused extensively on refining the window-based mechanism. For example, HAT [46] enlarged window sizes and used overlaps to enhance cross-window communication, while ELAN [47] and SRFormer [48] addressed computational redundancy. More sophisticated attention patterns were also developed, such as the sparse attention in DRSFormer [14], the strip attention in StripFormer [13], the transposed self-attention in Restormer [49], the integration of an adaptive token dictionary [50], and progressive focused attention [51]. Furthermore, hybrid models like GRL [52] and X-Restormer [53] have explored the fruitful combination of convolutional and attention-based feature extraction.

Alongside these core architectural advancements, several complementary research lines have gained traction. Emerging paradigms like state-space models, exemplified by MambaIR [54], [55], offer a practical solution for image restoration tasks. Meanwhile, Shi *et al.* [56] introduce the VmambaIR by the proposed omni-scan, and Li *et al.* [57] propose the MaIR with the local S-shape scanning and sequential shuffle attention. Besides, Wang *et al.* [58] exploited the vision autoregressive model for all-in-one image restoration. Moreover, researchers are exploring other critical facets of image restoration, such as estimating model uncertainty [59]–[62] and leveraging self-supervised pre-training with contrastive learning to derive robust image priors without paired data [63]–[66]. These diverse efforts collectively enrich the field and provide a strong foundation for tackling more complex restoration scenarios.

### B. All-in-One Image Restoration: The Quest for a Unified Model

Addressing the challenges of all-in-one image restoration, where a single model must gracefully handle diverse degradations, has inspired a variety of innovative strategies [5]. A significant body of work has focused on developing sophisticated prompting mechanisms to guide general-purpose backbones, adapting their behavior to specific tasks. This approach often involves learning adaptive prompts directly from the data. Influential works like AirNet [67] and PromptIR [15] demonstrated how a learned degradation representation can effectively modulate a restoration network. To enhance the discriminability of these prompts, subsequent methods introduced explicit regularization, such as the orthogonality constraints in IDR [68] and the frequency-domain regularization in AdaIR [16]. Rajagopalan *et al.* [69] exploit the task prompt representation with the in-context learning paradigm. Others have explored more expressive prompt representations, for instance, by modeling the prompt as a learned distribution as in DPPD [70]. A parallel thread in prompt-based learning injects richer semantic knowledge from large, pre-trained multimodal models. Zheng *et al.* [71] propose the deep unfolding model with pretrained multimodal prior. Methods like DA-CLIP [72], TextualDegRemoval [73], Perceive-IR [74], and OmniFuse [75] leverage models like CLIP [76] to provide textual or multimodal guidance. More recently, architectures leveraging Mixture-of-Experts (MoE), such as MoCE-IR [77], have been exploited to select specialized parameters for different restoration tasks.

Complementing the work on prompt-based guidance, another significant research direction investigates generative diffusion models [78], [79]. For instance, Özdenizci *et al.* [78] proposed the first diffusion-based deweathering model. Following this, Ye *et al.* [79] enhanced the diffusion framework with task-aware adapters to better address multiple degradation tasks. Besides, some research investigates the optimization challenges inherent in training a single model on diverse data. From a multi-task learning perspective, methods like [80] have explored techniques to mitigate task conflicts, while others like [81] focus on correcting for data and task bias during joint training. Similarly, contrastive learning has been adapted

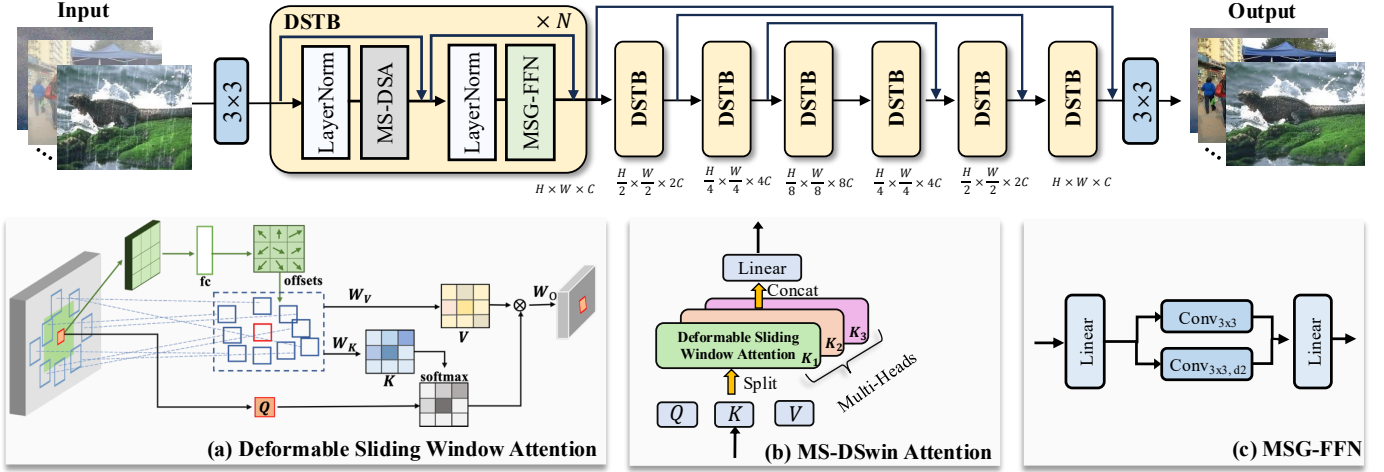


Fig. 3. Overview of the proposed DSwinIR architecture. The model is built upon a U-shaped backbone where the core component is the DSwin Transformer Block (DSTB). The key modules include: (a) Deformable Sliding Window Attention (DSwin), which adaptively samples features by learning content-dependent offsets; (b) Multi-Scale Deformable Sliding Window (MS-DSwin) Attention, which integrates multi-scale DSwin attention across multiple attention heads; and (c) Multi-Scale Gated Feed-Forward Network (MSG-FFN), which leverages parallel convolutional branches to enhance feature representation.

to the all-in-one setting to help the model better decouple degradation-specific features from content-invariant features [82], [83].

### C. Positioning Our Contribution

The power of content-adaptive receptive fields has been clearly established, first bringing significant gains to convolutional networks [84]. This principle was subsequently adapted for Transformer architectures, such as in the multi-scale deformable attention proposed by Zhu et al. [85] and the deformable attention mechanisms developed by Xia et al. [86]. Drawing inspiration from this clear line of progress, we introduce the Deformable Sliding Window (DSwin) Attention, a new paradigm that is both token-centric and content-aware. It directly addresses the core architectural flaws of prior window-based models by eliminating boundary artifacts and enabling content-adaptive receptive fields. By focusing on evolving the foundational architecture, our DSwinIR demonstrates that a sufficiently intelligent and adaptive backbone can achieve state-of-the-art performance, even surpassing prompt-based methods. Our work does not preclude the use of prompts; rather, it provides a significantly more powerful and robust foundation upon which future, more effective prompting strategies can be built.

## III. METHOD

In this section, we introduce DSwinIR. We first outline the overall architecture, then describe the progression from standard window attention to the proposed DSwin attention, including the motivation and formulation. Finally, we present the DSwin Transformer Block and a practical multi-scale design.

### A. Overall Architecture

We adopt a U-shaped encoder-decoder architecture with hierarchical feature processing (Fig. 3). The core of this

architecture is our novel DSwin Transformer Block, which we will detail in subsequent sections. The entire network is trained end-to-end, optimized with the  $L_1$  pixel-wise loss function, which encourages sharp and accurate predictions by penalizing the absolute difference between the restored output and the ground-truth image.

### B. From Window Attention to Deformable Sliding Window Attention

We revisit window-based attention and develop the Deformable Sliding Window (DSwin) attention from this perspective. In the following subsections, we outline the formulation and design choices.

#### 1) Preliminaries: Revisiting Window-based Self-Attention:

We first review standard window-based self-attention as depicted in Figure 1(c). A query token near the center may enjoy a full set of neighbors, but one at the edge—and especially a corner—is starved of context, blind to potentially crucial information just across the arbitrary window boundary. We refer to this as boundary blindness and aim to mitigate it. We briefly formalize its operation here to precisely identify the source of these inherent architectural flaws.

Given a 2D input feature map  $\mathbf{X} \in \mathbb{R}^{H \times W \times C}$ , standard window-based self-attention first partitions  $\mathbf{X}$  into a set of non-overlapping windows  $\{\mathbf{X}_w\}$ , where each window  $\mathbf{X}_w \in \mathbb{R}^{M \times M \times C}$  and  $M$  is the window size. Within each window, query ( $\mathbf{Q}_w$ ), key ( $\mathbf{K}_w$ ), and value ( $\mathbf{V}_w$ ) projections are computed. The self-attention is then calculated as:

$$\text{Attention}(\mathbf{Q}_w, \mathbf{K}_w, \mathbf{V}_w) = \text{Softmax} \left( \frac{\mathbf{Q}_w \mathbf{K}_w^T}{\sqrt{d}} + \mathbf{B} \right) \mathbf{V}_w, \quad (1)$$

where  $d$  is the head dimension and  $\mathbf{B}$  is a learnable relative position bias. As discussed in the introduction, this formulation, while efficient, inherently suffers from insufficient cross-window interaction.

2) *Token-Centric Sliding Window*: Boundary artifacts largely stem from non-overlapping partitions. We replace window-centric partitioning with a *token-centric* sliding window, inspired by sliding convolution.

For a given query token at position  $(i, j)$ , we define its local neighborhood of size  $k \times k$ . This operation extracts a feature patch  $\mathcal{N}_k(i, j) \in \mathbb{R}^{k \times k \times C}$  centered at each position  $(i, j)$ . It effectively transforms the feature map  $\mathbf{X}$  into a sequence of patches, where each patch contains the keys and values for a corresponding query token. The attention for the query token  $\mathbf{q}_{i,j}$  is then computed over the keys  $\mathbf{K}_{i,j}$  and values  $\mathbf{V}_{i,j}$  extracted from its neighborhood  $\mathcal{N}_k(i, j)$ :

$$\mathbf{Y}_{i,j}^{\text{slide}} = \sum_{(u,v) \in \mathcal{N}_k} \text{Softmax}_{uv} \left( \frac{\mathbf{q}_{i,j} \cdot \mathbf{k}_{i+u,j+v}}{\sqrt{d}} \right) \mathbf{v}_{i+u,j+v}, \quad (2)$$

where  $(u, v)$  are the relative coordinates within the  $k \times k$  neighborhood. Unlike non-overlapping windows, this sliding mechanism reduces the information bottleneck at boundaries and facilitates communication across spatial locations.

3) *Content-Aware Deformable Sampling*: Sliding windows alleviate boundary issues but still rely on a fixed, rectangular sampling grid. This fixed partitioning is misaligned with the arbitrary geometry of natural image structures and degradation patterns, such as the fine, diagonal lines of rain streaks or the amorphous, non-uniform nature of haze. Such a mismatch compromises the model’s ability to efficiently aggregate contextually relevant features, pointing to a critical need for a more flexible mechanism that can dynamically shape its receptive field in a content-aware manner.

a) *Offset Prediction and Differentiable Sampling*: For each query token  $\mathbf{q}_{i,j}$ , we predict a set of 2D spatial offsets  $\{\Delta \mathbf{p}_{i,j}^{(u,v)}\}$  for all  $k \times k$  sampling points in its neighborhood. These offsets are generated by a lightweight offset prediction network  $f_\theta$  that takes the query features as input:

$$\{\Delta \mathbf{p}_{i,j}^{(u,v)}\} = f_\theta(\mathbf{q}_{i,j}). \quad (3)$$

The network  $f_\theta$  is implemented as a lightweight module consisting of a depth-wise separable convolution, followed by a GELU activation function, and a final linear projection. No explicit offset regularization was required in our experiments; offsets are learned end-to-end via the restoration loss. The deformed key and value features are then sampled from the original feature map at the new coordinates  $(i + u + \Delta u_{i,j}^{(u,v)}, j + v + \Delta v_{i,j}^{(u,v)})$ . Since the offsets are fractional, we use *differentiable bilinear interpolation* to sample the features, ensuring the entire process is end-to-end trainable. A value at a fractional location  $(x, y)$  is computed as:

$$\mathbf{F}(x, y) = \sum_{i', j'} w(i', j') \cdot \mathbf{X}(\lfloor x \rfloor + i', \lfloor y \rfloor + j'), \quad (4)$$

where  $(i', j') \in \{(0, 0), (0, 1), (1, 0), (1, 1)\}$  are the four integer grid neighbors, and  $w(i', j')$  are the bilinear interpolation weights, which are proportional to the distance from  $(x, y)$  to the opposite corner.

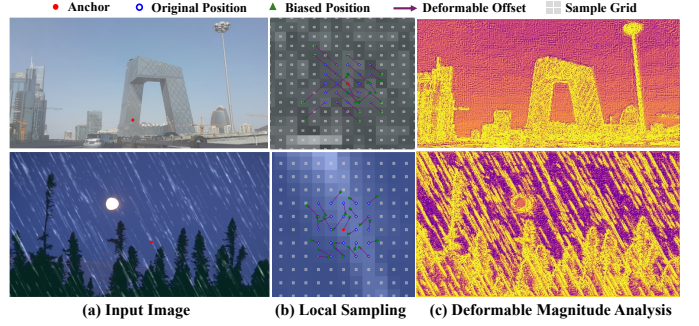


Fig. 4. Visualization of the content-aware sampling mechanism in DSwinIR. The figure presents a qualitative analysis of our proposed DSwin Attention. (a) The input image, with a red dot indicating the anchor location for local analysis. (b) The corresponding local sampling pattern, showing the reference grid, the adaptively sampled points, and the learned offsets. (c) The Deformation Magnitude Map, which visualizes the offset distance ( $d = \sqrt{dx^2 + dy^2}$ ) as a heatmap, where brighter intensity signifies a larger offset.

b) *Deformable Sliding Window Attention*: By combining these elements, the final Deformable Sliding Window (DSwin) Attention output for a token at position  $(i, j)$  is formulated as:

$$\mathbf{Y}_{i,j} = \sum_{(u,v) \in \mathcal{N}_k} \alpha_{i,j}^{(u,v)} \cdot \mathbf{v}_{\text{interp}}(i + u + \Delta u_{i,j}^{(u,v)}, j + v + \Delta v_{i,j}^{(u,v)}), \quad (5)$$

where  $\alpha_{i,j}^{(u,v)}$  represents the attention weights computed using the deformed keys, and  $\mathbf{v}_{\text{interp}}$  denotes the value sampled via bilinear interpolation. This formulation combines sliding and deformable sampling: sliding provides overlapping local context; deformable offsets adapt sampling to content, as illustrated in Figure 1(d).

### C. DSwin Transformer Block

The DSwin Transformer Block integrates DSwin attention and a feed-forward network with a complementary multi-scale strategy to strengthen feature extraction.

1) *Multi-Scale DSwin (MS-DSwin) Attention*: Image content and degradations manifest across a spectrum of scales. The standard multi-head attention framework provides a natural and computationally efficient vehicle for capturing such multi-scale information. Instead of treating all attention heads identically, we leverage this structure to explicitly assign different spatial extents to different groups of heads, as depicted in Figure 3(b). Specifically, for a model with  $N$  heads, we partition them into groups, with each group  $h$  being assigned a unique sliding window kernel size  $k_h$ . This allows the model to simultaneously aggregate features from both compact local neighborhoods and broader contextual regions within a single MS-DSwin module. Outputs from all heads are concatenated and projected to fuse multi-scale information at a small additional cost.

2) *Multi-Scale Gated Feed-Forward Network (MSG-FFN)*: A standard feed-forward network (FFN) processes tokens independently via point-wise linear layers, without explicit spatial context. To keep a multi-scale design throughout the block, we introduce a Multi-Scale Gated FFN (MSG-FFN): after channel expansion, features split into parallel depth-wise

TABLE I

COMPREHENSIVE OVERVIEW OF THE EXPERIMENTAL SETTINGS USED TO EVALUATE DSwinIR. EACH SETTING IS DEFINED BY ITS RESTORATION TASKS, DEGRADATION TYPES, AND CORRESPONDING DATASETS FOR TRAINING AND TESTING.

Experiment Settings	Tasks	Degradation Types	Datasets
Three-Task Restoration	3	Denoising, Dehazing, Deraining	BSD400 [87], WED [88], RESIDE (SOTS) [89], Rain100L [90], BSD68 [91]
Five-Task Restoration	5	Adds Motion Deblurring & Low-Light Enhancement to the three-task setup	Adds GoPro [92] and LOLv1 [93] to the three-task training set
Synthetic Deweathering	3	Snow, Raindrop, Outdoor Rain	Snow100K [94], Raindrop [95], Outdoor-Rain [96]
Real-World Deweathering	3	Real Rain, Real Snow, Real Haze	SPA-Data [97], RealSnow [98], REVIDE [99]
Real-World Deweathering	3	All-Time Adverse Weather Types	WeatherBench [100]
Composite Degradation	11	Low-Light, Haze, Rain, Snow, and their combinations	DIV2K [101] with corresponding degradations

convolution branches with different kernel sizes or dilations, followed by gating and projection. As shown in Figure 3(c), after an initial channel expansion layer, the MSG-FFN splits the features into parallel branches. Each branch employs a depth-wise convolution with a different kernel size or dilation rate, explicitly re-introducing spatial reasoning at multiple scales.

#### D. Remarks

It is crucial to position our contribution not as another incremental improvement, but as a complementary perspective in designing attention mechanisms for dense prediction tasks. Previous works typically resort to hand-crafted patterns. Our DSwin Attention, in contrast, introduces the token-centric and content-aware paradigm. This addresses the core issues of *cross-window interaction* and *inflexible receptive fields* directly and adaptively.

*Content-Aware Property:* To provide intuition for the dynamic behavior of our proposed DSwin Attention, we present a visual analysis of its learned offsets in Figure 4. This visualization highlights two key properties of our module. First, at a micro-level (middle column), the learned offsets enable the sampling points to break free from the rigid reference grid, allowing the module to adaptively fetch features from more informative, non-adjacent locations. Second, at a macro-level (right column), the module exhibits a strong content-aware capability. We visualize the offset magnitude ( $d = \sqrt{dx^2 + dy^2}$ ) as a heatmap and observe a clear correlation with input complexity. The module learns significantly larger offsets for challenging regions (e.g., complex textures or heavy degradation), indicating an active search for relevant information over a wider area. Conversely, it reverts to a local operation (minimal offsets) in simple, uniform regions. This behavior validates that our DSwin Attention operates as a dynamic, content-aware operator rather than a static receptive field expander. We provide a more quantitative analysis of the resulting receptive field in our ablation study.

## IV. EXPERIMENTS

In this section, we conduct a comprehensive set of experiments to rigorously evaluate the performance of our proposed DSwinIR. We first detail the experimental setup, including

datasets, evaluation protocols, and implementation specifics. We then present extensive quantitative and qualitative comparisons against state-of-the-art methods across a wide range of image restoration tasks. Finally, we provide in-depth ablation studies to dissect the contribution of each component of our model and analyze its underlying mechanisms.

#### A. Experimental Setup

To comprehensively validate the capabilities of DSwinIR, we have designed a multi-faceted evaluation protocol spanning a wide range of restoration scenarios, from standard multi-task benchmarks to complex and composite degradations. This section details the benchmarks, competing methods, and implementation specifics of our experiments.

1) *Evaluation Benchmarks and Metrics:* Our evaluation is structured across four distinct experimental settings, each designed to probe a specific aspect of our model’s performance. For all quantitative evaluations, we employ the widely-recognized Peak Signal-to-Noise Ratio (PSNR) and Structural Similarity Index Measure (SSIM). Higher values in both metrics indicate superior restoration quality.

a) *Multi-Task All-in-One Image Restoration:* This setting assesses the ability of a single model to serve as a versatile, general-purpose restorer. Following established conventions, we evaluate on two standard benchmarks. The *three-task* benchmark [15], [67] comprises Gaussian denoising, deraining, and dehazing. The more challenging *five-task* benchmark [16] extends this by incorporating motion deblurring and low-light enhancement, demanding greater generalization from a single set of model weights. The specific datasets for training and testing are detailed in Table I.

b) *Adverse Weather Removal:* This setting focuses on the practical and challenging domain of deweathering. We test DSwinIR’s robustness on both synthetic and real-world data. For the synthetic evaluation, we use the “AllWeather” collection [96], which includes images corrupted by snow, raindrops, and heavy rain, allowing for a controlled assessment across varied weather phenomena. To validate real-world efficacy, we employ a challenging benchmark [98] composed of datasets with authentic rain (SPA-Data [97]), snow (RealSnow [98]), and haze (REVIDE [99]), which feature complex, non-uniform artifacts that are the true test of a model’s generalization power.

TABLE II  
 QUANTITATIVE COMPARISONS FOR *Setting 1: three distinct degradation tasks*. \* DENOTES RESULTS REPORTED BY PRIOR WORK [15], [74].

Type	Method	Venue	Denoising (CBSD68 [91])			Dehazing	Deraining	Average
			$\sigma = 15$	$\sigma = 25$	$\sigma = 50$	SOTS [89]	Rain100L [90]	
General	MPRNet [7]	CVPR'21	33.27/0.920	30.76/0.871	27.29/0.761	28.00/0.958	33.86/0.958	30.63/0.894
	Uformer [11]	CVPR'22	33.55/0.922	30.71/0.859	27.63/0.786	27.13/0.953	34.28/0.961	30.66/0.896
	Restormer [49]	CVPR'22	33.72/0.930	30.67/0.865	27.63/0.792	27.78/0.958	33.78/0.958	30.75/0.901
	NAFNet [38]	ECCV'22	33.03/0.918	30.47/0.865	27.12/0.754	24.11/0.928	33.64/0.956	29.67/0.844
	FSNet* [39]	TPAMI'23	33.81/0.930	30.84/0.872	27.69/0.792	29.14/0.968	35.61/0.969	31.42/0.906
	DRSformer* [14]	CVPR'23	33.28/0.921	30.55/0.862	27.58/0.786	29.02/0.968	35.89/0.970	31.26/0.902
	MambaIR* [54]	ECCV'24	33.88/0.931	30.95/0.874	27.74/0.793	29.57/0.970	35.42/0.969	31.51/0.907
	VmambaIR [56]	TCSVT'25	33.75/0.927	31.10/0.879	27.81/0.782	29.75/0.970	35.63/0.970	31.61/0.906
	MaIR [57]	CVPR'25	33.60/0.925	30.98/0.876	27.69/0.779	28.94/0.965	34.52/0.964	31.15/0.902
All-in-One	DL [102]	TPAMI'19	33.05/0.914	30.41/0.861	26.90/0.740	26.92/0.391	32.62/0.931	29.98/0.875
	AirNet [67]	CVPR'22	33.92/0.932	31.26/0.888	28.00/0.797	27.94/0.962	34.90/0.967	31.20/0.910
	IDR* [68]	CVPR'23	33.89/0.931	31.32/0.884	28.04/0.798	29.87/0.970	36.03/0.971	31.83/0.911
	PromptIR [15]	NeurIPS'23	33.98/0.933	31.31/0.888	28.06/0.799	30.58/0.974	36.37/0.972	32.06/0.913
	Gridformer* [103]	IJCV'24	33.93/0.931	31.37/0.887	28.11/0.801	30.37/0.970	37.15/0.972	32.19/0.912
	NDR [104]	TIP'24	34.01/0.932	31.36/0.887	28.10/0.798	28.64/0.962	35.42/0.969	31.51/0.910
	InstructIR [105]	ECCV'24	<b>34.15/0.933</b>	31.52/0.890	<u>28.30/0.804</u>	30.22/0.959	37.98/0.978	32.43/0.913
	TextualDegRemoval [73]	CVPR'24	34.01/0.933	31.39/0.890	28.18/0.802	<u>31.63/0.980</u>	37.58/0.979	32.63/0.917
	AdaIR [16]	ICLR'25	34.12/0.935	31.45/0.892	28.19/0.802	31.06/0.980	<u>38.64/0.983</u>	32.69/0.918
	Perceive-IR [74]	TIP'25	34.13/0.934	<u>31.53/0.890</u>	<b>28.31/0.804</b>	<u>30.87/0.975</u>	38.29/0.980	32.63/0.917
	PoolNet [106]	TIP'25	34.10/0.935	31.45/0.892	28.18/0.803	30.94/0.980	<u>38.54/0.983</u>	32.64/0.919
	VLU-Net [71]	CVPR'25	34.13/0.935	31.48/0.892	28.23/0.804	30.71/0.980	<b>38.93/0.984</b>	<b>32.70/0.919</b>
	<b>DSwinIR (Ours)</b>	2025	34.12/0.933	<u><b>31.59/0.890</b></u>	<u><b>28.31/0.803</b></u>	<b>31.86/0.980</b>	<u>37.73/0.983</u>	<b>32.72/0.917</b>

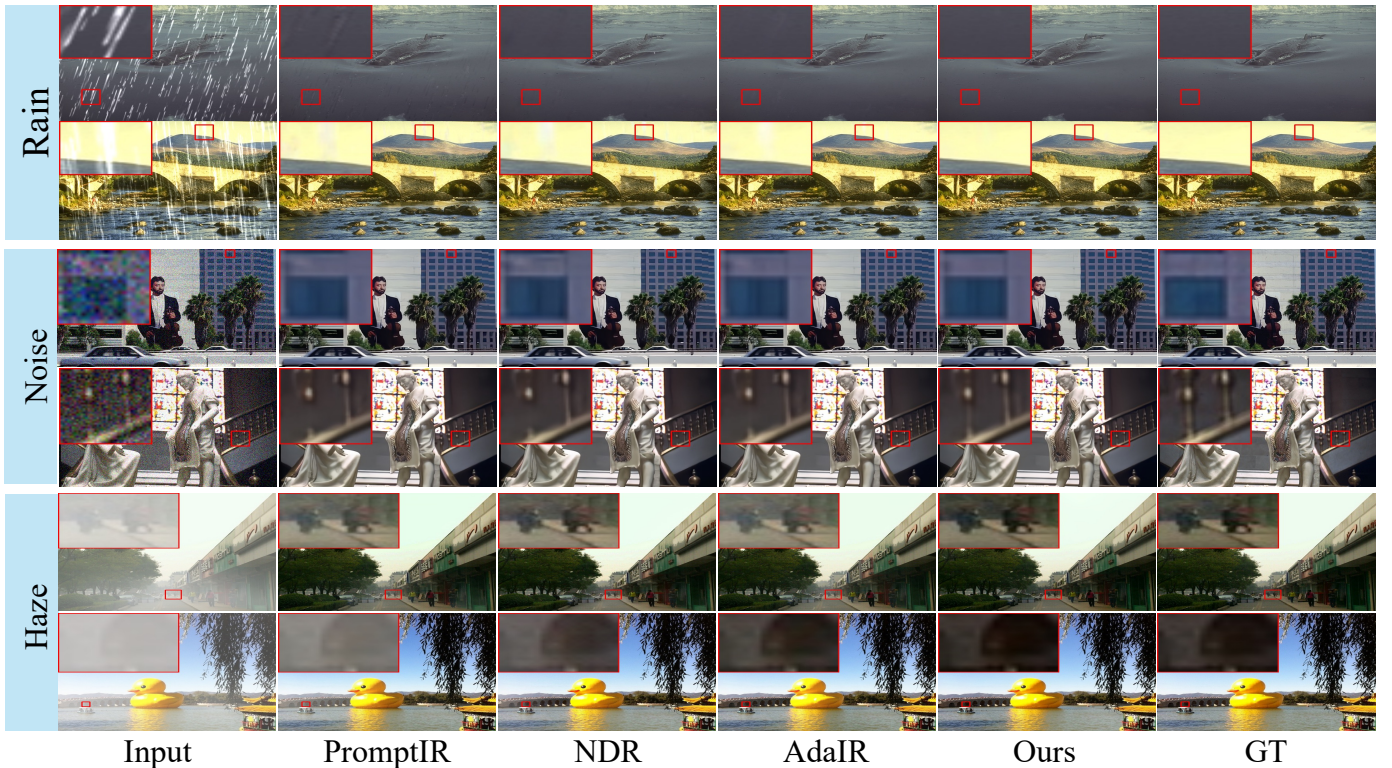


Fig. 5. Visual comparison of restoration results across three degradation tasks: noise removal (top row), rain streak removal (middle row), and dehazing (bottom row). Zoom-in regions (shown in colored boxes) demonstrate that our method achieves superior detail preservation and degradation removal.

To further validate our method, we also conduct evaluations on the recent WeatherBench [100] dataset. This large-scale, real-world benchmark provides 41,402 training and 600 testing

pairs. It presents a significant challenge by incorporating a diverse array of adverse weather conditions, including foggy, raining, and snowing scenarios captured during both daytime

TABLE III  
 QUANTITATIVE COMPARISONS FOR *Setting 2: five distinct degradation tasks*. \* INDICATES NUMBERS REPORTED BY PRIOR WORK [15], [74].

Type	Method	Venue	Denoising	Dehazing	Deraining	Deblurring	Low-Light	Average
			CBSD68 [91]	SOTS [89]	Rain100L [90]	GoPro [92]	LOL [93]	
General	SwinIR [10]	ICCVW'21	30.59/0.868	21.50/0.891	30.78/0.923	24.52/0.773	17.81/0.723	25.04/0.835
	Uformer [11]	CVPR'22	30.49/0.883	23.40/0.919	33.32/0.962	26.26/0.807	21.16/0.817	26.93/0.877
	MIRNet-v2 [107]	TPAMI'22	30.97/0.881	24.03/0.927	33.89/0.954	26.30/0.799	21.52/0.815	27.34/0.875
	Restormer [49]	CVPR'22	<u>31.49/0.884</u>	24.09/0.927	34.81/0.962	27.22/0.829	20.41/0.806	27.60/0.881
	NAFNet [38]	ECCV'22	31.02/0.883	25.23/0.939	35.56/0.967	26.53/0.808	20.49/0.809	27.76/0.881
	DRSformer* [14]	CVPR'23	30.97/0.881	24.66/0.931	33.45/0.953	25.56/0.780	21.77/0.821	27.28/0.873
	Retinexformer* [108]	ICCV'23	30.84/0.880	24.81/0.933	32.68/0.940	25.09/0.779	22.76/0.834	27.24/0.873
	FSNet* [39]	TPAMI'23	31.33/0.883	25.53/0.943	36.07/0.968	28.32/0.869	22.29/0.829	28.71/0.898
	MambaIR* [54]	ECCV'24	31.41/0.884	25.81/0.944	36.55/0.971	28.61/0.875	22.49/0.832	28.97/0.901
	VMambaIR [56]	TCSVT'25	30.81/0.879	27.65/0.949	34.26/0.960	26.02/0.799	22.38/0.827	28.22/0.883
MaIR [57]	CVPR'25	30.98/0.882	27.72/0.950	34.04/0.946	25.68/0.791	22.17/0.821	28.11/0.876	
All-in-One	DL [102]	TPAMI'19	23.09/0.745	20.54/0.826	21.96/0.762	19.86/0.672	19.83/0.712	21.05/0.743
	TAPE [109]	ECCV'22	30.18/0.855	22.16/0.861	29.67/0.904	24.47/0.763	18.97/0.621	25.09/0.801
	Transweather [110]	CVPR'22	29.00/0.841	21.32/0.885	29.43/0.905	25.12/0.757	21.21/0.792	25.22/0.836
	AirNet [67]	CVPR'22	30.91/0.882	21.04/0.884	32.98/0.951	24.35/0.781	18.18/0.735	25.49/0.846
	IDR [68]	CVPR'23	<b>31.60/0.887</b>	25.24/0.943	35.63/0.965	27.87/0.846	21.34/0.826	28.34/0.893
	PromptIR* [15]	NeurIPS'23	31.47/0.886	26.54/0.949	36.37/0.970	28.71/ <b>0.881</b>	22.68/0.832	29.15/0.904
	Gridformer* [103]	IJCV'24	31.45/0.885	26.79/0.951	36.61/0.971	<u>29.22/0.884</u>	22.59/0.831	29.33/0.904
	InstructIR [105]	ECCV'24	31.40/ <b>0.887</b>	27.10/0.956	36.84/0.973	<u>29.40/0.886</u>	<b>23.00/0.836</b>	29.55/0.907
	AdaIR [16]	ICLR'25	31.35/ <u>0.889</u>	<u>30.53/0.978</u>	<u>38.02/0.981</u>	28.12/0.858	<b>23.00/0.845</b>	<u>30.20/0.910</u>
	Perceive-IR [74]	TIP'25	31.44/ <b>0.887</b>	28.19/0.964	37.25/0.977	<b>29.46/0.886</b>	<u>22.88/0.833</u>	29.84/0.909
	PoolNet [106]	TIP'25	31.24/ <b>0.887</b>	30.25/0.977	37.85/ <u>0.981</u>	27.66/0.844	22.66/0.841	29.93/0.906
	VLU-Net [71]	CVPR'25	31.43/ <b>0.891</b>	<b>30.84/0.980</b>	<b>38.54/0.982</b>	27.46/0.840	22.29/0.833	30.11/0.905
	<b>DSwinIR (Ours)</b>	2025	31.34/0.885	30.09/0.975	37.77/ <b>0.982</b>	29.17/0.879	<u>22.64/0.843</u>	<b>30.20/0.913</b>

and nighttime.

*c) Composite Degradation:* To push the boundaries of evaluation, we evaluate a composite degradation benchmark introduced in [111] to assess the model’s performance in more realistic and complex scenarios where multiple corruptions coexist. This benchmark is crucial for testing a model’s ability to disentangle and simultaneously mitigate interacting artifacts. We adopt a challenging test set by combining four degradation types: low-light (l), haze (h), rain (r), and snow (s). The evaluation protocol includes all single degradations, all six dual-degradation combinations (e.g., l+h, h+r), and two triple-degradation combinations (l+h+r, l+h+s). Success in this setting signals a higher level of architectural intelligence and robustness.

*d) Single-Task Specialization:* While all-in-one models demonstrate versatility, a truly superior architecture must also excel when specialized. This experimental setting investigates the “specialization power” of DSwinIR by training it exclusively for a single task. We conduct focused evaluations on image deraining (Rain100L and the real-world SPA-Data) and dehazing (SOTS). In addition, we employ further low-light evaluation benchmarks, including the real-world LOLv2 dataset. We also evaluate DSwinIR on a mixed task involving both low-light enhancement and deblurring on the LowBlur dataset, following the protocol from [36]. Outperforming state-of-the-art specialist models in this context provides evidence of our architecture’s significant strength.

*2) Compared Methods:* To comprehensively position DSwinIR within the literature, we conduct extensive comparisons against a spectrum of state-of-the-art models. This includes foundational, backbone-centric architectures such as Uformer [11], Restormer [49], DRSformer [14], GridFormer [103], MambaIR [54], VmambaIR [56], and MaIR [57] allowing for a direct benchmark of the architectural efficacy of our proposed DSwin attention. Furthermore, we contrast our model with cutting-edge prompt-based and instruction-guided all-in-one methods, including AirNet [67], PromptIR [15], InstructIR [105], AdaIR [16], PoolNet [106], and VLUNet [71]. Demonstrating superiority over this class of models highlights that our DSwinIR provides a more powerful and efficient solution than methods reliant on external semantic guidance or task-specific modules.

*3) Implementation Details:* DSwinIR is trained end-to-end using the AdamW optimizer with an initial learning rate of  $2 \times 10^{-4}$ , which is decayed using a cosine annealing schedule. Our model employs a four-level U-shaped architecture, with the number of DSwin Transformer blocks in the encoder stages set to [4, 6, 6, 8] from shallow to deep. We use a batch size of 8 and train on randomly cropped  $128 \times 128$  patches from the respective training images. All experiments are conducted using PyTorch on 2 NVIDIA 3090 GPUs.

## B. Results and Analysis

In this section, we present a detailed analysis of DSwinIR’s performance across a hierarchy of benchmarks, ranging from

TABLE IV  
 QUANTITATIVE COMPARISONS FOR ADVERSE WEATHER REMOVAL INCLUDING RAIN, HAZE, AND SNOW. MISSING VALUES ARE DENOTED BY ‘—’.

Type	Methods	Venue	Snow100K-S [94]		Snow100K-L [94]		Outdoor-Rain [96]		RainDrop [95]		Average	
			PSNR	SSIM	PSNR	SSIM	PSNR	SSIM	PSNR	SSIM	PSNR	SSIM
Task-Specific	SPANet [97]	CVPR’19	29.92	0.8260	23.70	0.7930	—	—	—	—	—	—
	DesnowNet [94]	TIP’18	32.33	0.9500	27.17	0.8983	—	—	—	—	—	—
	HRGAN [112]	CVPR’19	—	—	—	—	21.56	0.8550	—	—	—	—
	MPRNet [7]	CVPR’21	—	—	—	—	28.03	0.9192	—	—	—	—
	AttentiveGAN [95]	CVPR’18	—	—	—	—	—	—	31.59	0.9170	—	—
	IDT [44]	TIP’22	—	—	—	—	—	—	31.87	0.9313	—	—
	NAFNet [38]	ECCV’22	34.79	0.9497	30.06	0.9017	29.59	0.9027	—	—	—	—
	Restormer [49]	CVPR’22	36.01	0.9579	30.36	0.9068	30.03	0.9215	32.18	0.9408	—	—
All-in-One	All-in-One [113]	CVPR’20	—	—	28.33	0.8820	24.71	0.8980	31.12	0.9268	28.05	0.9023
	TransWeather [110]	CVPR’22	32.51	0.9341	29.31	0.8879	28.83	0.9000	30.17	0.9157	30.20	0.9094
	Chen <i>et al.</i> [114]	CVPR’22	34.42	0.9469	30.22	0.9071	29.27	0.9147	31.81	0.9309	31.43	0.9249
	WGWSNet [115]	CVPR’22	34.31	0.9460	30.16	0.9007	29.32	0.9207	32.38	0.9378	31.54	0.9263
	WeatherDiff <sub>64</sub> [78]	TPAMI’23	35.83	0.9566	30.09	0.9041	29.64	0.9312	30.71	0.9312	31.57	0.9308
	WeatherDiff <sub>128</sub> [78]	TPAMI’23	35.02	0.9516	29.58	0.8941	29.72	0.9216	29.66	0.9225	31.00	0.9225
	AWRCP [116]	ICCV’23	36.92	0.9652	31.92	<b>0.9341</b>	31.39	0.9329	31.93	0.9314	33.04	0.9409
	GridFormer [103]	IJCV’24	<u>37.46</u>	0.9640	31.71	0.9231	31.87	0.9335	32.39	0.9362	33.36	0.9392
	MPerceiver [117]	CVPR’24	36.23	0.9571	31.02	0.9164	31.25	0.9246	<b>33.21</b>	0.9294	32.93	0.9319
	DTPM [79]	CVPR’24	37.01	<u>0.9663</u>	30.92	0.9174	30.99	0.9340	32.72	0.9440	32.91	0.9404
	Histoformer [118]	ECCV’24	37.41	0.9656	<u>32.16</u>	0.9261	<u>32.08</u>	<u>0.9389</u>	<u>33.06</u>	<u>0.9441</u>	<u>33.68</u>	<u>0.9437</u>
	<b>DSwinIR (Ours)</b>	2025	<b>38.11</b>	<b>0.9683</b>	<b>32.58</b>	<u>0.9312</u>	<b>32.76</b>	<b>0.9502</b>	32.88	<b>0.9474</b>	<b>34.08</b>	<b>0.9493</b>

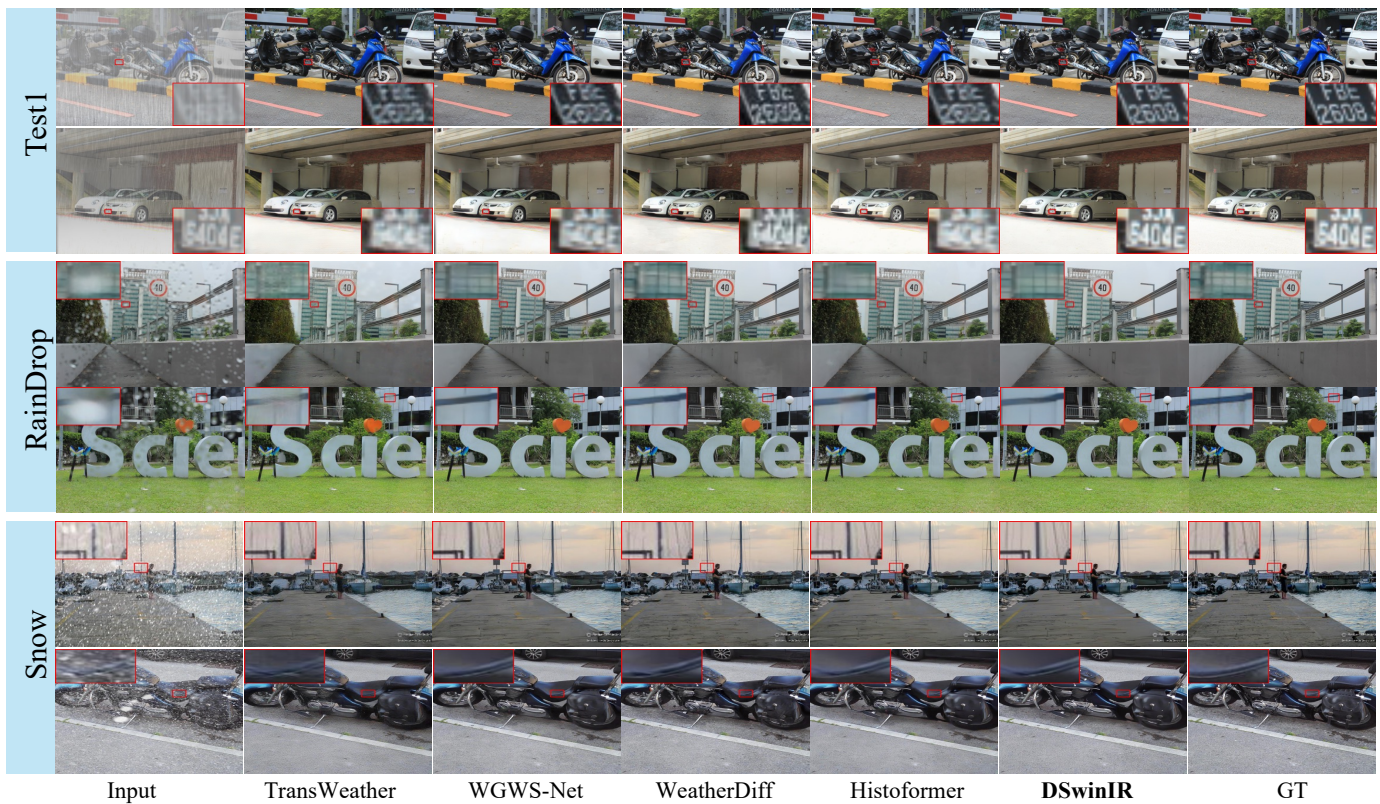


Fig. 6. Visual results on the AllWeather datasets; from top to bottom are samples for outdoor-rain, raindrop and snow test data. Our DSwinIR achieves better clarity even when compared to the diffusion-based approaches.

complex multi-degradation scenarios to specialized single-task settings. Our aim is not only to establish the state-of-the-art performance of our model but also to provide insights into the architectural and mechanistic factors that contribute to its effectiveness. In the following result tables, **Best** and **second-best** results are highlighted.

1) *Results on All-in-One Image Restoration*: The most challenging test for any restoration model is the all-in-one setting, where a single network must handle a diverse array of degradations. We evaluate DSwinIR on the standard three-task and five-task benchmarks to demonstrate its capacity as a powerful universal backbone.

a) *Performance on Three Degradation Tasks*: Following the classic benchmark setup [15], [67], we first evaluate on denoising, deraining, and dehazing. The quantitative results are presented in Table II. DSwinIR achieves an average PSNR of 32.72 dB. This result demonstrates improvements over other foundational architectures like GridFormer (32.19 dB) and validates the efficacy of our DSwin attention. Furthermore, DSwinIR remains highly competitive even when compared to the latest prompt-based (e.g., AdaIR, 32.69 dB) and multimodal (e.g., VLUNet, 32.70 dB) methods. The ability of our vision-only backbone to perform at this level suggests its strong intrinsic representation power. The qualitative results in Figure 5 are consistent with these quantitative findings, showing that DSwinIR effectively restores fine textures and removes complex artifacts.

b) *Performance on Five Degradation Tasks*: To further probe the model’s generalization, we adopt the five-task benchmark, which introduces deblurring and low-light enhancement tasks. As detailed in Table III, DSwinIR achieves an average PSNR of 30.20 dB. This result is highly competitive with the top-performing methods, such as the prompt-based AdaIR (30.20 dB). The model’s performance is notably strong in tasks requiring significant spatial transformation, such as deraining (e.g., +0.93 dB over InstructIR) and dehazing (e.g., +2.99 dB over InstructIR). While its performance on low-light enhancement is competitive rather than leading, its overall strength across the other tasks secures this high average. This highlights the DSwinIR architecture’s ability to jointly learn from a diverse set of degradations within a single set of weights.

2) *Results on Deweathering Datasets*: Beyond general restoration, we investigate DSwinIR’s performance in the practical domain of deweathering, which requires handling complex, real-world atmospheric phenomena.

a) *Synthetic Deweathering Benchmarks*: On the comprehensive AllWeather dataset collection, which includes snow, raindrops, and outdoor rain, DSwinIR demonstrates clear superiority. As presented in Table IV, our model achieves an average PSNR of 34.08 dB, surpassing the previous best, Histoformer [118], by a convincing margin of 0.4 dB. The visual results in Figure 6 are consistent with the quantitative results. Compared to prior works, including diffusion-based models, DSwinIR consistently produces images with better clarity, more vibrant colors, and sharper details, effectively removing weather artifacts without introducing secondary distortions.

TABLE V  
COMPARISON ON DE-WEATHERING TASKS ON REAL-WORLD DATASETS FOLLOWING [98]

Datasets	Methods	PSNR $\uparrow$	SSIM $\uparrow$
SPA+	Chen et al. [114]	37.32	<u>0.97</u>
	TransWeather [110]	33.64	0.93
	WGWSNet [98]	<u>38.94</u>	<b>0.98</b>
	<b>DSwinIR (Ours)</b>	<b>40.60</b>	<b>0.98</b>
RealSnow	Chen et al. [114]	29.37	<u>0.88</u>
	TransWeather [110]	29.16	0.82
	WGWSNet [98]	<u>29.46</u>	0.85
	<b>DSwinIR (Ours)</b>	<b>30.14</b>	<b>0.89</b>
REVIDE	Chen et al. [114]	20.10	0.85
	TransWeather [110]	17.33	0.82
	WGWSNet [98]	<u>20.44</u>	<u>0.87</u>
	<b>DSwinIR (Ours)</b>	<b>20.80</b>	<b>0.89</b>
Average	Chen et al. [114]	28.93	<u>0.90</u>
	TransWeather [110]	26.71	0.86
	WGWSNet [98]	<u>29.61</u>	<u>0.90</u>
	<b>DSwinIR (Ours)</b>	<b>30.51</b>	<b>0.92</b>

b) *Real-World Deweathering Benchmarks*: On a challenging benchmark composed of real-world rain, snow, and haze datasets [98], DSwinIR again performs well. As shown in Table V, our model achieves an average PSNR of 30.51 dB, significantly outperforming the previous state-of-the-art WGWSNet [98] by 0.9 dB.

Moreover, we conduct evaluations on the recent, large-scale real-world WeatherBench dataset [100], with results presented in Table VI. Our method, DSwinIR, achieves competitive overall performance. Notably, DSwinIR performs well in the Dehaze and Desnow tasks, outperforming the next-best method (MWFormer) by 0.73 dB in Dehaze PSNR and 0.14 dB in Desnow PSNR. While WGWS-Net shows strong performance in Derain, our model achieves a close second-best result. This performance across all categories results in a high overall average, indicating a good balance and robustness across diverse weather conditions. As illustrated in Figure 7, the qualitative results are consistent with these quantitative findings. DSwinIR effectively removes complex weather artifacts (e.g., dense fog, heavy snow) while preserving fine-grained details and avoiding color casts.

3) *Results on Composite Degradations*: We evaluate DSwinIR on the challenging composite degradation benchmark (CDD-11) [111], which features 11 combinations of low-light, haze, rain, and snow. As presented in Table VII, our DSwinIR achieves an average PSNR of 29.43 dB, which is 0.96 dB higher than the next-best method, OneRestore [111]. The proposed DSwinIR can learn to adapt its receptive field to different degradation structures (e.g., thin rain streaks or broad haze), and our model achieves the advanced performance across all 11 individual and combined degradation settings, demonstrating the architecture’s robustness in handling complex, interacting artifacts. The qualitative results in Figure 8 are consistent with these quantitative findings, showing that DSwinIR effectively removes interacting artifacts while preserving image detail.

TABLE VI  
QUANTITATIVE COMPARISON ON THE REAL-WORLD WEATHERBENCH DATASET.

Type	Method	Venue	Dehaze			Derain			Desnow			Average		
			PSNR $\uparrow$	SSIM $\uparrow$	LPIPS $\downarrow$	PSNR $\uparrow$	SSIM $\uparrow$	LPIPS $\downarrow$	PSNR $\uparrow$	SSIM $\uparrow$	LPIPS $\downarrow$	PSNR $\uparrow$	SSIM $\uparrow$	LPIPS $\downarrow$
General	DehazeFormer [119]	TIP'23	24.12	0.745	0.345	36.05	0.954	0.181	28.88	0.849	0.178	29.68	0.849	0.235
	DCMPNet [120]	CVPR'24	21.18	0.506	0.491	32.04	0.876	0.282	24.81	0.614	0.546	26.01	0.665	0.440
	DRSformer [14]	CVPR'23	19.95	0.694	0.404	33.98	0.943	0.209	28.00	0.836	0.197	27.31	0.824	0.270
	NeRD-Rain [121]	CVPR'24	21.52	0.718	0.386	35.74	0.950	0.182	28.87	0.851	0.182	28.71	0.840	0.250
	SnowFormer [122]	arXiv'22	22.71	0.736	<u>0.305</u>	35.18	0.951	0.155	29.30	0.868	<u>0.143</u>	29.06	0.852	<u>0.201</u>
	MPRNet [37]	CVPR'21	23.27	0.739	0.355	36.14	0.954	0.171	29.18	0.860	0.177	29.53	0.851	0.234
	Restormer [49]	CVPR'22	19.30	0.687	0.412	34.49	0.945	0.197	27.95	0.836	0.197	27.25	0.823	0.269
All-in-One	AirNet [67]	CVPR'22	20.94	0.705	0.383	33.59	0.942	0.224	22.06	0.780	0.291	25.53	0.809	0.299
	TransWeather [110]	CVPR'22	19.79	0.680	0.397	29.34	0.903	0.294	24.96	0.796	0.231	24.70	0.793	0.307
	WGWS-Net [98]	CVPR'23	13.79	0.603	0.535	<u>37.08</u>	<b>0.961</b>	<b>0.117</b>	20.81	0.780	0.248	23.89	0.781	0.300
	PromptIR [15]	NeurIPS'23	21.11	0.713	0.375	34.54	0.944	0.198	27.93	0.836	0.195	27.86	0.831	0.256
	DiffUIR [123]	CVPR'24	22.74	0.744	0.355	35.93	<u>0.955</u>	0.172	29.50	0.870	0.162	29.39	<u>0.856</u>	0.230
	MWFormer [124]	TIP'24	24.42	0.746	<b>0.284</b>	35.15	0.951	<u>0.153</u>	29.98	<u>0.872</u>	<b>0.133</b>	29.85	<u>0.856</u>	<b>0.190</b>
	Histoformer [118]	ECCV'24	17.69	0.669	0.437	30.70	0.916	0.279	25.39	0.808	0.225	24.59	0.798	0.314
	AdaIR [16]	ICLR'25	23.08	0.731	0.351	34.87	0.946	0.192	28.44	0.837	0.179	28.80	0.838	0.240
	<b>DSwinIR (Ours)</b>	2025	<b>25.15</b>	<b>0.766</b>	0.329	<b>37.17</b>	<b>0.961</b>	0.173	<b>30.12</b>	<b>0.873</b>	0.170	<b>30.81</b>	<b>0.867</b>	0.224

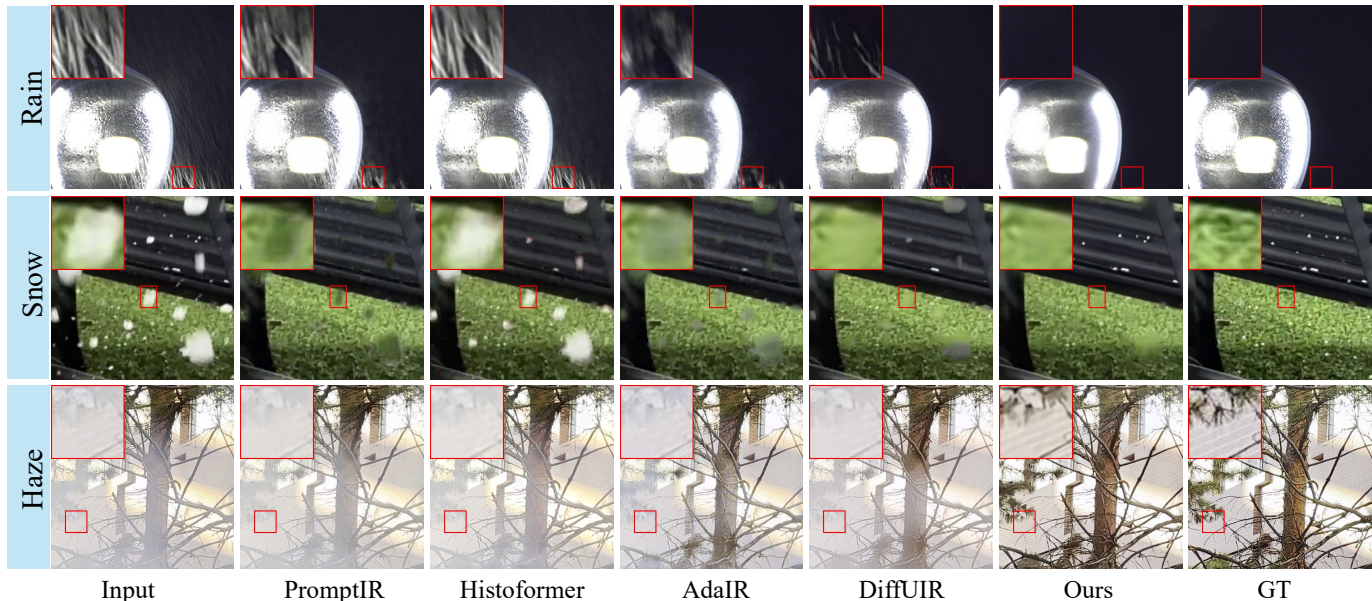


Fig. 7. Visual results on the real-world WeatherBench dataset.

4) *Results on Single-Task Settings:* To complement the all-in-one results, we also investigate the performance of DSwinIR on single-task benchmarks. These experiments are designed to assess the model’s effectiveness when its architecture is optimized for a single task, and to benchmark its performance against models developed specifically for these applications.

a) *Deraining on Rain100L:* We first evaluate the model’s performance on the standard Rain100L benchmark. As shown in Table VIII, this is a highly competitive field. When trained solely for this task, DSwinIR demonstrates strong performance. The gain over other backbone architectures like PromptIR (+1.98 dB) suggests the architectural progress provided by our DSwin attention. Moreover, DSwinIR also achieves a 0.12 dB improvement over the recent AdaIR model.

b) *Dehazing on SOTS Outdoor:* The task of single-image dehazing presents a different challenge, often requiring a nuanced understanding of both global atmospheric light and local object details. As detailed in Table IX, DSwinIR achieves a PSNR of 32.89 dB. This result represents a 1.09 dB gain over the next-best method, AdaIR. We posit that the deformable mechanism’s ability to adapt its receptive field is well-suited to the non-homogeneous nature of haze, while the sliding mechanism’s capacity to preserve fine structural details ensures object clarity.

c) *Real-World Deraining on SPA-Data:* We also test DSwinIR on the real-world SPA-Data benchmark. The results, summarized in Table XII, show DSwinIR achieves a PSNR of 49.19 dB. This represents a 0.66 dB gain over the strong

TABLE VII  
QUANTITATIVE RESULTS ON THE COMPOSITE DEGRADATION SETTING.

Method	Venue	l	h	r	s	l+h	l+r	l+s	h+r	h+s	l+h+r	l+h+s	Avg.
Restormer [49]	CVPR'22	26.29	28.35	33.10	33.43	24.80	25.28	24.99	26.80	26.15	23.90	23.82	26.99
NAFNet [38]	ECCV'22	24.50	25.34	29.24	29.54	21.91	22.75	22.79	23.67	23.86	21.03	20.82	24.13
AirNet [67]	CVPR'22	24.83	24.21	26.55	26.79	23.23	22.82	23.29	22.21	23.29	21.80	22.24	23.75
PromptIR [15]	NeurIPS'23	26.32	26.10	31.56	31.53	24.49	25.05	24.51	24.54	23.70	23.74	23.33	25.90
TransWeather [110]	CVPR'22	23.39	23.95	26.69	25.74	22.24	22.62	21.80	23.10	22.34	21.55	21.01	23.13
WeatherDiff [98]	TPAMI'23	23.58	21.99	24.85	24.80	21.83	22.69	22.12	21.25	21.99	21.23	21.04	22.49
WGWSNet [98]	CVPR'23	24.39	27.90	33.15	34.43	24.27	25.06	24.60	27.23	27.65	23.90	23.97	26.96
InstructIR [105]	ECCV'24	<u>26.70</u>	<u>32.61</u>	<u>33.51</u>	34.45	24.36	25.41	<u>25.63</u>	28.80	29.64	24.84	24.32	28.21
OneRestore [111]	ECCV'24	26.55	<u>32.71</u>	33.48	<u>34.50</u>	<u>26.15</u>	<u>25.83</u>	<u>25.56</u>	<u>30.27</u>	<u>30.46</u>	<u>25.18</u>	<u>25.28</u>	<u>28.47</u>
<b>DSwinIR (Ours)</b>	2025	<b>27.38</b>	<b>33.72</b>	<b>34.95</b>	<b>35.44</b>	<b>26.56</b>	<b>26.54</b>	<b>26.24</b>	<b>30.94</b>	<b>30.54</b>	<b>25.70</b>	<b>25.70</b>	<b>29.43</b>

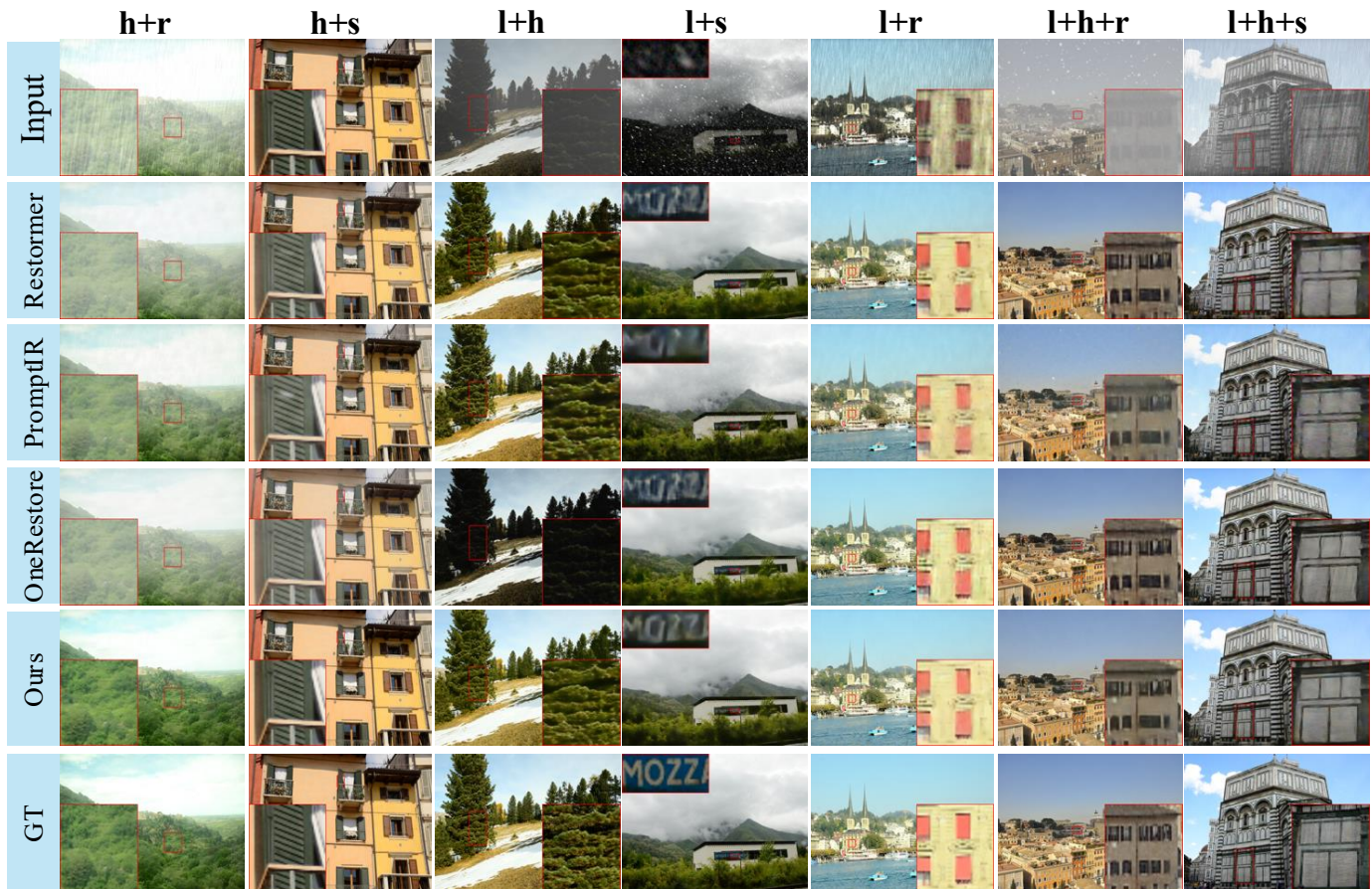


Fig. 8. Visual results on the composite degradation tasks, showcasing performance on mixed degradations. Our method more effectively mitigates multiple interacting degradations, restoring clearer images with improved color fidelity and detail.

DRSformer model. It suggests that the DSwin attention’s ability to learn adaptive, data-driven receptive fields provides a practical advantage for tackling such complex, non-uniform degradations.

*d) Low-Light Image Enhancement:* We first evaluate DSwinIR on the widely-used low-light enhancement benchmark, LOLv2, which includes both real-world (LOLv2-Real) and synthetic (LOLv2-Syn) test sets. As presented in Table X, our model achieves state-of-the-art performance on both subsets. Furthermore, to assess the model’s capability in handling

complex, compound degradations, we evaluate DSwinIR on the mixed task of joint low-light enhancement and deblurring. Following the experimental setup of DarkIR [36] on the LowBlur dataset, our model again demonstrates superior performance, as detailed in Table XI. DSwinIR achieves the highest scores with 27.33 dB in PSNR and 0.909 in SSIM. These results underscore the strong generalization capability of our model for the dedicated low-light enhancement task.

TABLE VIII  
SINGLE-TASK DERAINING RESULTS ON THE RAIN100L DATASET.

Method	DIDMDN [125]	UMR [126]	SIRR [127]	MSPFN [29]	LPNet [128]	AirNet [67]	Restormer [49]	PromptIR [15]	AdaIR [16]	<b>DSwinIR (Ours)</b>
PSNR	23.79	32.39	32.37	33.50	33.61	34.90	36.74	37.04	38.90	<b>39.02</b>
SSIM	0.773	0.921	0.926	0.948	0.958	0.977	0.978	0.979	0.985	<b>0.986</b>

TABLE IX  
SINGLE-TASK DEHAZING RESULTS ON THE SOTS OUTDOOR TEST SET.

Method	DehazeNet [24]	MSCNN [129]	AODNet [130]	EPDN [131]	FDGAN [132]	AirNet [67]	Restormer [49]	PromptIR [15]	AdaIR [16]	<b>DSwinIR (Ours)</b>
PSNR	22.46	22.06	20.29	22.57	23.15	23.18	30.87	31.31	31.80	<b>32.89</b>
SSIM	0.851	0.908	0.877	0.863	0.921	0.900	0.969	0.973	0.981	<b>0.984</b>

TABLE X  
QUANTITATIVE COMPARISON ON THE LOLV2 DATASET [133] FOR LOW-LIGHT ENHANCEMENT.

Method	LOLv2-Real		LOLv2-Syn	
	PSNR	SSIM $\uparrow$	PSNR $\uparrow$	SSIM
RetinexNet [134]	15.47	0.567	17.13	0.798
UFormer [11]	18.82	0.771	19.66	0.871
FIDE [135]	16.85	0.678	15.20	0.612
DRBN [136]	20.29	0.831	23.22	0.927
KinD [137]	14.74	0.641	13.29	0.578
Restormer [49]	19.94	0.827	21.41	0.830
MIRNet [138]	20.02	0.820	21.94	0.876
SNR-Net [139]	21.48	0.849	24.14	0.928
FourLLIE [140]	21.60	0.847	24.17	0.917
Retinexformer [108]	<u>22.80</u>	0.840	<u>25.67</u>	<u>0.930</u>
<b>DSwinIR (Ours)</b>	<b>23.17</b>	<b>0.851</b>	<b>25.74</b>	<b>0.934</b>

### C. Ablation Study

To validate our design choices and rigorously quantify the contribution of each proposed component, we conduct a series of in-depth ablation studies. We use the challenging three-task all-in-one setting as our testbed and present the comprehensive results in Figure 9.

*a) Efficacy of the Core DSwin Mechanisms:* To validate our design, we incrementally introduce our components starting from established baselines. The Uformer [11] and DRSformer [14] models provide benchmarks at 30.66 dB and 31.26 dB, respectively. Our first experiment, isolating the sliding window mechanism, yields 31.79 dB, confirming the effectiveness of the token-centric paradigm. In parallel, isolating the deformable window mechanism achieves 32.11 dB, a result that already outperforms the prompt-based PromptIR baseline (32.06 dB). When these two components are combined, the resulting DSwin module ( $K=7$ ) achieves 32.53 dB. This performance gain is greater than the sum of the individual component improvements, demonstrating a clear synergistic effect.

*b) Effective Receptive Field and Efficiency:* The visualizations of the receptive field in Figure 10 offer profound qualitative insights into why DSwinIR is so effective. Its receptive field is demonstrably both global in reach and local in precision. This is the direct result of our design principles: the sliding mechanism ensures a connected, expansive base, while the deformable mechanism learns to dynamically concentrate attention on areas like object contours and textures.

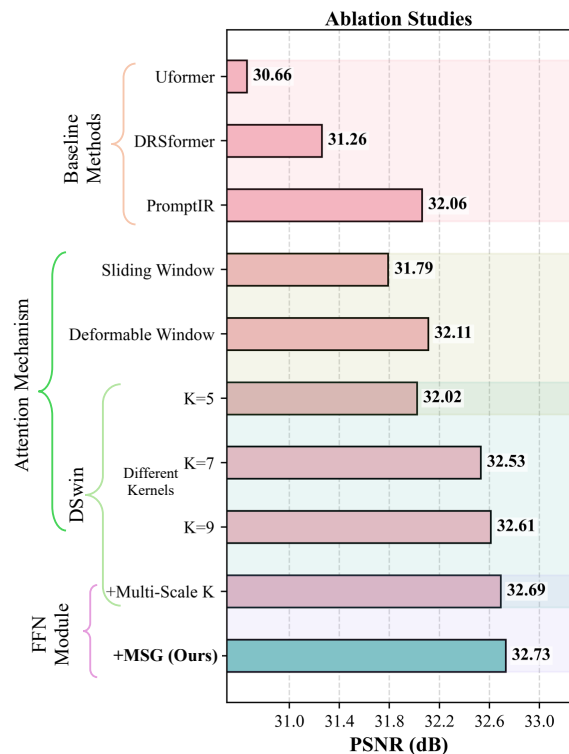


Fig. 9. Ablation studies demonstrating the effectiveness of our key components. We evaluate (1) different attention mechanisms, showing improvements from sliding window (31.79 dB) and Deformable Window (32.11 dB) over baselines; (2) DSwin configurations with various kernel sizes ( $K=5, 7, 9$ ) and multi-scale enhancement (32.69 dB); and (3) FFN module with MSG enhancement, achieving the best performance (32.72 dB). All experiments report the average PSNR of three distinct degradation tasks.

Moreover, DSwinIR also exhibits computational efficiency, as detailed in Table XIII. It is crucial to note that DSwinIR achieves its superior performance without substantially increasing computational cost. Compared to its top-performing competitors, DSwinIR is significantly more economical. For instance, it requires 15% fewer FLOPs and is 22% faster than PromptIR, while delivering a substantially higher PSNR. The advantage is even more dramatic when compared to DRSformer, against which DSwinIR uses about 40% fewer FLOPs.

*c) Impact of Kernel Size and Multi-Scale Strategy:* Having validated the DSwin concept, we next investigate its optimal configuration. We first analyze the impact of a fixed

TABLE XI  
QUANTITATIVE COMPARISON FOR THE MIXED TASK (LOW-LIGHT ENHANCEMENT AND DEBLURRING) ON THE LOWBLUR DATASET [141].

Method	KinD++ [137]	DRBN [136]	DeblurGAN-v2 [142]	MIMO [143]	NAFNet [38]	LEDNet [144]	RetinexFormer [108]	Restormer [49]	DarkIR [36]	<b>DSwinIR (Ours)</b>
PSNR	21.26	21.78	22.30	22.41	25.36	25.74	26.02	26.72	<u>27.30</u>	<b>27.33</b>
SSIM	0.753	0.768	0.745	0.835	0.882	0.850	0.887	<u>0.902</u>	0.898	<b>0.909</b>

TABLE XII  
SINGLE-TASK DERAISING RESULTS ON THE REAL-WORLD SPA-DATA DATASET.

Method	MSPFN [29]	MPRNet [37]	DualGCN [145]	SPDNet [146]	Uformer [11]	Restormer [49]	IDT [44]	DRSformer [14]	<b>DSwinIR (Ours)</b>
PSNR	43.43	43.64	44.18	43.20	46.13	47.98	47.35	48.53	<b>49.19</b>
SSIM	0.9843	0.9844	0.9902	0.9871	0.9913	0.9921	<u>0.9930</u>	0.9924	<b>0.9938</b>

TABLE XIII  
EFFICIENCY EVALUATION OF DIFFERENT METHODS WITH  $256 \times 256$  INPUT.

Methods	Core Operation	Params.	FLOPs	Latency	PSNR
AirNet [67]	Deformable Conv	9M	301G	0.57s	31.20
Uformer [11]	Window Attention	20M	41G	0.45s	30.66
Restormer [49]	Transposed Self-Attention	26M	155G	0.67s	30.75
PromptIR [15]	Trans. SA + Prompts	36M	173G	0.71s	32.06
DRSformer [14]	Sparse Window Attention	33M	243G	0.82s	31.26
<b>DSwinIR (Ours)</b>	<b>DSwin Attention</b>	<b>24M</b>	<b>147G</b>	<b>0.55s</b>	<b>32.72</b>

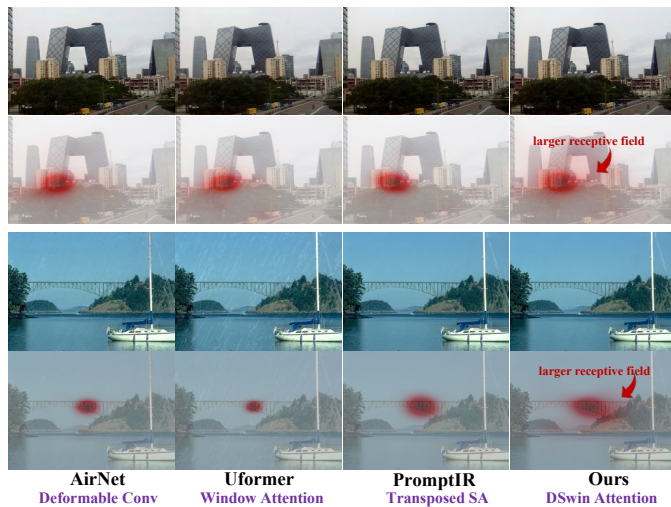


Fig. 10. Visualization of receptive fields of multiple backbones by LAM [147].

kernel size, testing  $K=5$ ,  $K=7$ , and  $K=9$ . The results show a clear trend: performance improves from 32.02 dB ( $K=5$ ) to 32.53 dB ( $K=7$ ), and then begins to plateau at 32.61 dB ( $K=9$ ). This suggests a trade-off, where a larger receptive field is beneficial, but excessively large kernels may not provide proportionally greater returns for their computational cost. This observation motivates our multi-scale strategy. By employing multi-scale kernels within a single attention module (+Multi-Scale  $K$ ), we reach a PSNR of 32.69 dB. This result is superior to even the best-performing single-kernel model ( $K=9$ ), providing clear evidence that empowering the model to simultaneously perceive features at multiple scales is more effective than relying on a single, large-but-fixed receptive field.

*d) Contribution of the Multi-Scale Gated FFN:* Finally, we analyze the feed-forward network. Incorporating our proposed multi-scale gated FFN (+MSG) yields the model’s peak performance at 32.72 dB. While this incremental gain is modest, it confirms the benefit of maintaining a holistic multi-scale philosophy across the entire Transformer block.

#### D. Discussion and Limitation

The extensive experiment results support the view that redesigning window attention with sliding and deformable sampling is effective across various benchmarks. Despite its demonstrated strengths, our work also illuminates several promising avenues for future research. First, while our architecture excels at restoring spatial structure, its performance on tasks dominated by extreme photometric adjustments, such as low-light enhancement, is competitive rather than leading. A promising future direction is to integrate explicit global photometric modeling, for instance, by combining our powerful backbone with lightweight techniques like 3D Look-Up Tables (3D-LUTs) or by incorporating a learnable codebook prior. Second, our focus on architectural innovation means adapting DSwinIR to new tasks requires full retraining. A compelling direction is to integrate our backbone with parameter-efficient fine-tuning (PEFT) techniques, creating systems that are both powerful and highly adaptable. Finally, we believe the core principles of token-centric, content-adaptive attention hold significant potential beyond restoration, offering a promising new building block for other dense prediction tasks like semantic segmentation and object detection, where the ability to dynamically model features is paramount.

#### V. CONCLUSION

In this paper, we revisit window-based self-attention for image restoration and propose the Deformable Sliding Window (DSwin) attention and the DSwinIR backbone. The token-centric sliding window reduces boundary effects by centering each token within its local context, while deformable sampling adapts the receptive field to image content. Extensive evaluations on all-in-one and single-task benchmarks show consistent improvements, including state-of-the-art results on several datasets. We hope DSwin will serve as a useful building block for future image restoration architectures and related dense prediction tasks.

## REFERENCES

- [1] M. Elad, B. Kwar, and G. Vaksman, "Image denoising: The deep learning revolution and beyond - A survey paper," *SIAM J. Imaging Sci.*, vol. 16, no. 3, pp. 1594–1654, 2023.
- [2] J. Gui, X. Cong, Y. Cao, W. Ren, J. Zhang, J. Cao, and D. Tao, "A comprehensive survey and taxonomy on single image dehazing based on deep learning," *ACM Comput. Surv.*, vol. 55, no. 13s, 2023.
- [3] X. Chen, J. Pan, J. Dong, and J. Tang, "Towards unified deep image deraining: A survey and a new benchmark," *IEEE Trans. Pattern Anal. Mach. Intell.*, vol. 47, no. 7, pp. 5414–5433, 2025.
- [4] K. Zhang, W. Ren, W. Luo, W. Lai, B. Stenger, M. Yang, and H. Li, "Deep image deblurring: A survey," *Int. J. Comput. Vis.*, vol. 130, no. 9, pp. 2103–2130, 2022.
- [5] J. Jiang, Z. Zuo, G. Wu, K. Jiang, and X. Liu, "A survey on all-in-one image restoration: Taxonomy, evaluation and future trends," *IEEE Trans. Pattern Anal. Mach. Intell.*, vol. 47, no. 12, pp. 11 892–11 911, 2025.
- [6] K. Zhang, W. Zuo, Y. Chen, D. Meng, and L. Zhang, "Beyond a gaussian denoiser: Residual learning of deep cnn for image denoising," *IEEE Trans. Image Process.*, vol. 26, no. 7, pp. 3142–3155, 2017.
- [7] S. W. Zamir, A. Arora, S. H. Khan, M. Hayat, F. S. Khan, M.-H. Yang, and L. Shao, "Multi-stage progressive image restoration," in *IEEE Conf. Comput. Vis. Pattern Recog.*, 2021, pp. 14 821–14 831.
- [8] A. Dosovitskiy, L. Beyer, A. Kolesnikov, D. Weissenborn, X. Zhai, T. Unterthiner, M. Dehghani, M. Minderer, G. Heigold, S. Gelly, J. Uszkoreit, and N. Houlsby, "An image is worth 16x16 words: Transformers for image recognition at scale," in *Int. Conf. Learn. Represent.*, 2021.
- [9] Z. Liu, Y. Lin, Y. Cao, H. Hu, Y. Wei, Z. Zhang, S. Lin, and B. Guo, "Swin transformer: Hierarchical vision transformer using shifted windows," in *Int. Conf. Comput. Vis.*, 2021, pp. 9992–10002.
- [10] J. Liang, J. Cao, G. Sun, K. Zhang, L. V. Gool, and R. Timofte, "SwinIR: Image restoration using swin transformer," in *Int. Conf. Comput. Vis. Workshops*, 2021, pp. 1833–1844.
- [11] Z. Wang, X. Cun, J. Bao, W. Zhou, J. Liu, and H. Li, "Uformer: A general u-shaped transformer for image restoration," in *IEEE Conf. Comput. Vis. Pattern Recog.*, 2022, pp. 17 662–17 672.
- [12] Z. Chen, Y. Zhang, J. Gu, Y. Zhang, L. Kong, and X. Yuan, "Cross aggregation transformer for image restoration," in *Adv. Neural Inform. Process. Syst.*, 2022.
- [13] F. Tsai, Y. Peng, Y. Lin, C. Tsai, and C. Lin, "Stripformer: Strip transformer for fast image deblurring," in *Eur. Conf. Comput. Vis.*, vol. 13679, 2022, pp. 146–162.
- [14] X. Chen, H. Li, M. Li, and J. Pan, "Learning a sparse transformer network for effective image deraining," in *IEEE Conf. Comput. Vis. Pattern Recog.*, 2023, pp. 5896–5905.
- [15] V. Potlapalli, S. W. Zamir, S. H. Khan, and F. S. Khan, "Promptir: Prompting for all-in-one image restoration," in *Adv. Neural Inform. Process. Syst.*, 2023.
- [16] Y. Cui, S. W. Zamir, S. H. Khan, A. Knoll, M. Shah, and F. S. Khan, "Adair: Adaptive all-in-one image restoration via frequency mining and modulation," in *Int. Conf. Learn. Represent.*, 2025.
- [17] M. Banham and A. Katsaggelos, "Digital image restoration," *IEEE Signal Processing Magazine*, vol. 14, no. 2, pp. 24–41, 1997.
- [18] Y. Almalioglu, M. Turan, N. Trigoni, and A. Markham, "Deep learning-based robust positioning for all-weather autonomous driving," *Nature Machine Intelligence*, vol. 4, pp. 749–760, 2022.
- [19] X. Xu, X. Yuan, Z. Wang, K. Zhang, and R. Hu, "Rank-in-rank loss for person re-identification," *ACM Trans. Multim. Comput. Commun. Appl.*, vol. 18, pp. 1–21, 2022.
- [20] C. Stringer and M. Pachitariu, "Cellpose3: one-click image restoration for improved cellular segmentation," *Nature Methods*, vol. 22, pp. 592–599, 2025.
- [21] A. M. Ali, B. Benjdira, A. Koubaa, W. El-Shafai, Z. Khan, and W. Boulila, "Vision transformers in image restoration: A survey," *Sensors*, vol. 23, no. 5, 2023.
- [22] C. Dong, C. C. Loy, K. He, and X. Tang, "Image super-resolution using deep convolutional networks," *IEEE Trans. Pattern Anal. Mach. Intell.*, vol. 38, no. 2, pp. 295–307, 2016.
- [23] X. Fu, J. Huang, X. Ding, Y. Liao, and J. W. Paisley, "Clearing the skies: A deep network architecture for single-image rain removal," *IEEE Trans. Image Process.*, vol. 26, no. 6, pp. 2944–2956, 2017.
- [24] B. Cai, X. Xu, K. Jia, C. Qing, and D. Tao, "Dehazenet: An end-to-end system for single image haze removal," *IEEE Trans. Image Process.*, vol. 25, no. 11, pp. 5187–5198, 2016.
- [25] B. Lim, S. Son, H. Kim, S. Nah, and K. M. Lee, "Enhanced deep residual networks for single image super-resolution," in *IEEE Conf. Comput. Vis. Pattern Recog. Workshops*, 2017, pp. 1132–1140.
- [26] Y. Zhang, Y. Tian, Y. Kong, B. Zhong, and Y. Fu, "Residual dense network for image super-resolution," in *IEEE Conf. Comput. Vis. Pattern Recog.*, June 2018, pp. 2472–2481.
- [27] Y. Zhang, K. Li, K. Li, L. Wang, B. Zhong, and Y. Fu, "Image super-resolution using very deep residual channel attention networks," in *Eur. Conf. Comput. Vis.*, 2018, pp. 294–310.
- [28] Y. Mei, Y. Fan, and Y. Zhou, "Image super-resolution with non-local sparse attention," in *IEEE Conf. Comput. Vis. Pattern Recog.*, 2021, pp. 3517–3526.
- [29] K. Jiang, Z. Wang, P. Yi, C. Chen, B. Huang, Y. Luo, J. Ma, and J. Jiang, "Multi-scale progressive fusion network for single image deraining," in *IEEE Conf. Comput. Vis. Pattern Recog.*, 2020, pp. 8346–8355.
- [30] S. Ni, X. Cao, T. Yue, and X. Hu, "Controlling the rain: From removal to rendering," in *IEEE Conf. Comput. Vis. Pattern Recog.*, 2021, pp. 6328–6337.
- [31] M. Zhou, J. Xiao, Y. Chang, X. Fu, A. Liu, J. Pan, and Z. Zha, "Image de-raining via continual learning," in *IEEE Conf. Comput. Vis. Pattern Recog.*, 2021, pp. 4907–4916.
- [32] X. Chen, J. Pan, and J. Dong, "Bidirectional multi-scale implicit neural representations for image deraining," in *IEEE Conf. Comput. Vis. Pattern Recog.*, 2024, pp. 25 627–25 636.
- [33] X. Qin, Z. Wang, Y. Bai, X. Xie, and H. Jia, "Ffa-net: Feature fusion attention network for single image dehazing," in *AAAI Conf. Artif. Intell.*, 2020, pp. 11 908–11 915.
- [34] Y. Cui, W. Ren, X. Cao, and A. Knoll, "Focal network for image restoration," in *Int. Conf. Comput. Vis.*, 2023, pp. 12 955–12 965.
- [35] B. Li, Y. Gou, W. Wang, P. Hu, W. Zuo, and X. Peng, "Relationship quantification of image degradations," *IEEE Trans. Pattern Anal. Mach. Intell.*, pp. 1–12, 2025.
- [36] D. Feijoo, J. C. Benito, Á. García, and M. V. Conde, "Darkir: Robust low-light image restoration," in *IEEE Conf. Comput. Vis. Pattern Recog.*, 2025, pp. 10 879–10 889.
- [37] S. W. Zamir, A. Arora, S. H. Khan, M. Hayat, F. S. Khan, M. Yang, and L. Shao, "Multi-stage progressive image restoration," in *IEEE Conf. Comput. Vis. Pattern Recog.*, 2021, pp. 14 821–14 831.
- [38] L. Chen, X. Chu, X. Zhang, and J. Sun, "Simple baselines for image restoration," in *Eur. Conf. Comput. Vis.*, vol. 13667, 2022, pp. 17–33.
- [39] Y. Cui, W. Ren, X. Cao, and A. Knoll, "Image restoration via frequency selection," *IEEE Trans. Pattern Anal. Mach. Intell.*, vol. 46, no. 2, pp. 1093–1108, 2024.
- [40] Y. Cui, W. Ren, S. Yang, X. Cao, and A. Knoll, "IRNeXt: Rethinking convolutional network design for image restoration," in *Int. Conf. Mach. Learn.*, vol. 202, 2023, pp. 6545–6564.
- [41] Y. Cui, W. Ren, X. Cao, and A. Knoll, "Revitalizing convolutional network for image restoration," *IEEE Trans. Pattern Anal. Mach. Intell.*, vol. 46, no. 12, pp. 9423–9438, 2024.
- [42] Z. Jin, Y. Qiu, K. Zhang, H. Li, and W. Luo, "Mb-taylorformer v2: Improved multi-branch linear transformer expanded by taylor formula for image restoration," *IEEE Trans. Pattern Anal. Mach. Intell.*, vol. 47, no. 7, pp. 5990–6005, 2025.
- [43] H. Chen, Y. Wang, T. Guo, C. Xu, Y. Deng, Z. Liu, S. Ma, C. Xu, C. Xu, and W. Gao, "Pre-trained image processing transformer," in *IEEE Conf. Comput. Vis. Pattern Recog.*, 2021, pp. 12 299–12 310.
- [44] J. Xiao, X. Fu, A. Liu, F. Wu, and Z. Zha, "Image de-raining transformer," *IEEE Trans. Pattern Anal. Mach. Intell.*, vol. 45, no. 11, pp. 12 978–12 995, 2023.
- [45] Y. Song, Z. He, H. Qian, and X. Du, "Vision transformers for single image dehazing," *IEEE Trans. Image Process.*, vol. 32, pp. 1927–1941, 2023.
- [46] X. Chen, X. Wang, J. Zhou, Y. Qiao, and C. Dong, "Activating more pixels in image super-resolution transformer," in *IEEE Conf. Comput. Vis. Pattern Recog.*, 2023, pp. 22 367–22 377.
- [47] X. Zhang, H. Zeng, S. Guo, and L. Zhang, "Efficient long-range attention network for image super-resolution," in *Eur. Conf. Comput. Vis.*, vol. 13677, 2022, pp. 649–667.
- [48] Y. Zhou, Z. Li, C. Guo, S. Bai, M. Cheng, and Q. Hou, "Srformer: Permuted self-attention for single image super-resolution," in *Int. Conf. Comput. Vis.*, 2023, pp. 12 734–12 745.
- [49] S. W. Zamir, A. Arora, S. Khan, M. Hayat, F. S. Khan, and M.-H. Yang, "Restormer: Efficient transformer for high-resolution image restoration," in *IEEE Conf. Comput. Vis. Pattern Recog.*, 2022, pp. 5718–5729.

- [50] L. Zhang, Y. Li, X. Zhou, X. Zhao, and S. Gu, "Transcending the limit of local window: Advanced super-resolution transformer with adaptive token dictionary," in *IEEE Conf. Comput. Vis. Pattern Recog.*, 2024, pp. 2856–2865.
- [51] W. Long, X. Zhou, L. Zhang, and S. Gu, "Progressive focused transformer for single image super-resolution," in *IEEE Conf. Comput. Vis. Pattern Recog.*, 2025.
- [52] Y. Li, Y. Fan, X. Xiang, D. Demandolx, R. Ranjan, R. Timofte, and L. V. Gool, "Efficient and explicit modelling of image hierarchies for image restoration," in *IEEE Conf. Comput. Vis. Pattern Recog.*, 2023, pp. 18 278–18 289.
- [53] X. Chen, Z. Li, Y. Pu, Y. Liu, J. Zhou, Y. Qiao, and C. Dong, "A comparative study of image restoration networks for general backbone network design," in *Eur. Conf. Comput. Vis.*, vol. 15129, 2024, pp. 74–91.
- [54] H. Guo, J. Li, T. Dai, Z. Ouyang, X. Ren, and S.-T. Xia, "Mambair: A simple baseline for image restoration with state-space model," in *ECCV*, 2024, pp. 222–241.
- [55] H. Guo, Y. Guo, Y. Zha, Y. Zhang, W. Li, T. Dai, S. Xia, and Y. Li, "Mambairv2: Attentive state space restoration," in *IEEE Conf. Comput. Vis. Pattern Recog.*, 2025.
- [56] Y. Shi, B. Xia, X. Jin, X. Wang, T. Zhao, X. Xia, X. Xiao, and W. Yang, "Vmambair: Visual state space model for image restoration," *IEEE Trans. Circuit Syst. Video Technol.*, vol. 35, no. 6, pp. 5560–5574, 2025.
- [57] B. Li, H. Zhao, W. Wang, P. Hu, Y. Gou, and X. Peng, "Mair: A locality- and continuity-preserving mamba for image restoration," in *IEEE Conf. Comput. Vis. Pattern Recog.*, 2025, pp. 7491–7501.
- [58] S. Wang and F. Zhao, "Navigating image restoration with var's distribution alignment prior," in *IEEE Conf. Comput. Vis. Pattern Recog.*, 2025.
- [59] Q. Ning, W. Dong, X. Li, J. Wu, and G. Shi, "Uncertainty-driven loss for single image super-resolution," in *Adv. Neural Inform. Process. Syst.*, 2021, pp. 16 398–16 409.
- [60] M. Hong, J. Liu, C. Li, and Y. Qu, "Uncertainty-driven dehazing network," in *AAAI Conf. Artif. Intell.*, 2022, pp. 906–913.
- [61] H. Huang, M. Luo, and R. He, "Memory uncertainty learning for real-world single image deraining," *IEEE Trans. Pattern Anal. Mach. Intell.*, vol. 45, no. 3, pp. 3446–3460, 2023.
- [62] Y. Qiao, M. Shao, X. Tan, and L. Meng, "Uncertainty-aware diffusion model for real-world image dehazing," in *Int. Conf. Mach. Learn.*, 2024, pp. 65–70.
- [63] H. Wu, Y. Qu, S. Lin, J. Zhou, R. Qiao, Z. Zhang, Y. Xie, and L. Ma, "Contrastive learning for compact single image dehazing," in *IEEE Conf. Comput. Vis. Pattern Recog.*, 2021, pp. 10 551–10 560.
- [64] Y. Zheng, J. Zhan, S. He, J. Dong, and Y. Du, "Curricular contrastive regularization for physics-aware single image dehazing," in *IEEE Conf. Comput. Vis. Pattern Recog.*, 2023, pp. 5785–5794.
- [65] X. Chen, J. Pan, K. Jiang, Y. Li, Y. Huang, C. Kong, L. Dai, and Z. Fan, "Unpaired deep image deraining using dual contrastive learning," in *IEEE Conf. Comput. Vis. Pattern Recog.*, 2022, pp. 2007–2016.
- [66] G. Wu, J. Jiang, K. Jiang, and X. Liu, "Learning from history: Task-agnostic model contrastive learning for image restoration," in *AAAI Conf. Artif. Intell.*, 2024, pp. 5976–5984.
- [67] B. Li, X. Liu, P. Hu, Z. Wu, J. Lv, and X. Peng, "All-in-one image restoration for unknown corruption," in *IEEE Conf. Comput. Vis. Pattern Recog.*, 2022, pp. 17 431–17 441.
- [68] J. Zhang, J. Huang, M. Yao, Z. Yang, H. Yu, M. Zhou, and F. Zhao, "Ingredient-oriented multi-degradation learning for image restoration," in *IEEE Conf. Comput. Vis. Pattern Recog.*, 2023, pp. 5825–5835.
- [69] S. Rajagopalan and V. M. Patel, "Awracle: All-weather image restoration using visual in-context learning," in *AAAI Conf. Artif. Intell.*, 2025, pp. 6675–6683.
- [70] G. Wu, J. Jiang, K. Jiang, X. Liu, and L. Nie, "Learning dynamic prompts for all-in-one image restoration," *IEEE Trans. Image Process.*, vol. 34, pp. 3997–4010, 2025.
- [71] H. Zeng, X. Wang, Y. Chen, J. Su, and J. Liu, "Vision-language gradient descent-driven all-in-one deep unfolding networks," in *IEEE Conf. Comput. Vis. Pattern Recog.*, 2025, pp. 7524–7533.
- [72] Z. Luo, F. K. Gustafsson, Z. Zhao, J. Sjölund, and T. B. Schön, "Controlling vision-language models for multi-task image restoration," in *Int. Conf. Learn. Represent.*, 2024.
- [73] T. Ye, S. Chen, W. Chai, Z. Xing, J. Qin, G. Lin, and L. Zhu, "Learning diffusion texture priors for image restoration," in *IEEE Conf. Comput. Vis. Pattern Recog.*, 2024, pp. 2524–2534.
- [74] X. Zhang, J. Ma, G. Wang, Q. Zhang, H. Zhang, and L. Zhang, "Perceive-ir: Learning to perceive degradation better for all-in-one image restoration," 2025.
- [75] H. Zhang, L. Cao, X. Zuo, Z. Shao, and J. Ma, "Omnifuse: Composite degradation-robust image fusion with language-driven semantics," *IEEE Trans. Pattern Anal. Mach. Intell.*, pp. 1–18, 2025.
- [76] A. Radford, J. W. Kim, C. Hallacy, A. Ramesh, G. Goh, S. Agarwal, G. Sastry, A. Askell, P. Mishkin, J. Clark, G. Krueger, and I. Sutskever, "Learning transferable visual models from natural language supervision," in *Int. Conf. Mach. Learn.*, vol. 139, 2021, pp. 8748–8763.
- [77] E. Zamfir, Z. Wu, N. Mehta, Y. Tan, D. P. Paudel, Y. Zhang, and R. Timofte, "Complexity experts are task-discriminative learners for any image restoration," in *IEEE Conf. Comput. Vis. Pattern Recog.*, 2025.
- [78] O. Özdenizci and R. Legenstein, "Restoring vision in adverse weather conditions with patch-based denoising diffusion models," *IEEE Trans. Pattern Anal. Mach. Intell.*, vol. 45, no. 8, pp. 10 346–10 357, 2023.
- [79] T. Ye, S. Chen, W. Chai, Z. Xing, J. Qin, G. Lin, and L. Zhu, "Learning diffusion texture priors for image restoration," in *IEEE Conf. Comput. Vis. Pattern Recog.*, 2024, pp. 2524–2534.
- [80] G. Wu, J. Jiang, K. Jiang, and X. Liu, "Harmony in diversity: Improving all-in-one image restoration via multi-task collaboration," in *ACM Int. Conf. Multimedia*, 2024, pp. 6015–6023.
- [81] G. Wu, J. Jiang, Y. Wang, K. Jiang, and X. Liu, "Debiased all-in-one image restoration with task uncertainty regularization," in *AAAI Conf. Artif. Intell.*, 2025, pp. 8386–8394.
- [82] X. Tang, X. Gu, X. He, X. Hu, and J. Sun, "Degradation-aware residual-conditioned optimal transport for unified image restoration," *IEEE Trans. Pattern Anal. Mach. Intell.*, pp. 1–16, 2025.
- [83] G. Wu, J. Jiang, K. Jiang, X. Liu, and L. Nie, "Beyond degradation redundancy: Contrastive prompt learning for all-in-one image restoration," *CoRR*, vol. abs/2504.09973, 2025.
- [84] J. Dai, H. Qi, Y. Xiong, Y. Li, G. Zhang, H. Hu, and Y. Wei, "Deformable convolutional networks," in *Int. Conf. Comput. Vis.* IEEE Computer Society, 2017, pp. 764–773.
- [85] X. Zhu, W. Su, L. Lu, B. Li, X. Wang, and J. Dai, "Deformable DETR: deformable transformers for end-to-end object detection," in *Int. Conf. Learn. Represent.*, 2021.
- [86] Z. Xia, X. Pan, S. Song, L. E. Li, and G. Huang, "Vision transformer with deformable attention," in *IEEE Conf. Comput. Vis. Pattern Recog.*, 2022, pp. 4784–4793.
- [87] P. Arbelaez, M. Maire, C. Fowlkes, and J. Malik, "Contour detection and hierarchical image segmentation," *IEEE Trans. Pattern Anal. Mach. Intell.*, vol. 33, no. 5, pp. 898–916, 2011-05.
- [88] K. Ma, Z. Duanmu, Q. Wu, Z. Wang, H. Yong, H. Li, and L. Zhang, "Waterloo exploration database: New challenges for image quality assessment models," *IEEE Trans. Image Process.*, vol. 26, no. 2, pp. 1004–1016, 2017-02.
- [89] B. Li, W. Ren, D. Fu, D. Tao, D. Feng, W. Zeng, and Z. Wang, "Benchmarking single-image dehazing and beyond," *IEEE Trans. Image Process.*, vol. 28, no. 1, pp. 492–505, 2019.
- [90] W. Yang, R. T. Tan, J. Feng, J. Liu, Z. Guo, and S. Yan, "Deep joint rain detection and removal from a single image," in *IEEE Conf. Comput. Vis. Pattern Recog.*, 2017, pp. 1685–1694.
- [91] D. R. Martin, C. C. Fowlkes, D. Tal, and J. Malik, "A database of human segmented natural images and its application to evaluating segmentation algorithms and measuring ecological statistics," in *Int. Conf. Comput. Vis.*, vol. 2, 2001, pp. 416–423.
- [92] S. Nah, T. H. Kim, and K. M. Lee, "Deep multi-scale convolutional neural network for dynamic scene deblurring," in *IEEE Conf. Comput. Vis. Pattern Recog.*, 2017, pp. 257–265.
- [93] C. Wei, W. Wang, W. Yang, and J. Liu, "Deep retinex decomposition for low-light enhancement," in *Brit. Mach. Vis. Conf.*, 2018, p. 155.
- [94] Y. Liu, D. Jaw, S. Huang, and J. Hwang, "Desnownet: Context-aware deep network for snow removal," *IEEE Trans. Image Process.*, vol. 27, no. 6, pp. 3064–3073, 2018.
- [95] R. Qian, R. T. Tan, W. Yang, J. Su, and J. Liu, "Attentive generative adversarial network for raindrop removal from a single image," in *IEEE Conf. Comput. Vis. Pattern Recog.*, 2018, pp. 2482–2491.
- [96] R. Li, L. Cheong, and R. T. Tan, "Heavy rain image restoration: Integrating physics model and conditional adversarial learning," in *IEEE Conf. Comput. Vis. Pattern Recog.*, 2019, pp. 1633–1642.
- [97] T. Wang, X. Yang, K. Xu, S. Chen, Q. Zhang, and R. W. H. Lau, "Spatial attentive single-image deraining with a high quality real rain dataset," in *IEEE Conf. Comput. Vis. Pattern Recog.*, 2019, pp. 12 270–12 279.

- [98] Y. Zhu, T. Wang, X. Fu, X. Yang, X. Guo, J. Dai, Y. Qiao, and X. Hu, "Learning weather-general and weather-specific features for image restoration under multiple adverse weather conditions," in *IEEE Conf. Comput. Vis. Pattern Recog.*, 2023, pp. 21 747–21 758.
- [99] X. Zhang, H. Dong, J. Pan, C. Zhu, Y. Tai, C. Wang, J. Li, F. Huang, and F. Wang, "Learning to restore hazy video: A new real-world dataset and a new method," in *IEEE Conf. Comput. Vis. Pattern Recog.*, 2021, pp. 9239–9248.
- [100] Q. Guan, Q. Yang, X. Chen, T. Song, G. Jin, and J. Jin, "Weatherbench: A real-world benchmark dataset for all-in-one adverse weather image restoration," *ACM Int. Conf. Multimedia*, 2025.
- [101] E. Agustsson and R. Timofte, "Ntire 2017 challenge on single image super-resolution: Dataset and study," in *IEEE Conf. Comput. Vis. Pattern Recog. Workshops*, 2017.
- [102] Q. Fan, D. Chen, L. Yuan, G. Hua, N. Yu, and B. Chen, "A general decoupled learning framework for parameterized image operators," *IEEE Trans. Pattern Anal. Mach. Intell.*, vol. 43, no. 1, pp. 33–47, 2021.
- [103] G. R. dense transformer with grid structure for image restoration in adverse weather conditions, "Gridformer: Residual dense transformer with grid structure for image restoration in adverse weather conditions," *Int. J. Comput. Vis.*, pp. 1–23, 2024.
- [104] M. Yao, R. Xu, Y. Guan, J. Huang, and Z. Xiong, "Neural degradation representation learning for all-in-one image restoration," *IEEE Trans. Image Process.*, vol. 33, pp. 5408–5423, 2024.
- [105] M. V. Conde, G. Geigle, and R. Timofte, "High-quality image restoration following human instructions," in *Eur. Conf. Comput. Vis.*, 2024, pp. 1–12.
- [106] Y. Cui, W. Ren, and A. Knoll, "Exploring the potential of pooling techniques for universal image restoration," *IEEE Trans. Image Process.*, vol. 34, pp. 3403–3416, 2025.
- [107] S. W. Zamir, A. Arora, S. Khan, M. Hayat, F. S. Khan, M.-H. Yang, and L. Shao, "Learning enriched features for fast image restoration and enhancement," *IEEE Trans. Pattern Anal. Mach. Intell.*, vol. 45, no. 2, pp. 1934–1948, 2022.
- [108] Y. Cai, H. Bian, J. Lin, H. Wang, R. Timofte, and Y. Zhang, "Retinex-former: One-stage retinex-based transformer for low-light image enhancement," in *Int. Conf. Comput. Vis.*, 2023, pp. 12 470–12 479.
- [109] L. Liu, L. Xie, X. Zhang, S. Yuan, X. Chen, W. Zhou, H. Li, and Q. Tian, "TAPE: task-agnostic prior embedding for image restoration," in *Eur. Conf. Comput. Vis.*, vol. 13678, 2022, pp. 447–464.
- [110] J. M. J. Valanarasu, R. Yasarla, and V. M. Patel, "Transweather: Transformer-based restoration of images degraded by adverse weather conditions," in *IEEE Conf. Comput. Vis. Pattern Recog.*, 2022, pp. 2343–2353.
- [111] Y. Guo, Y. Gao, Y. Lu, R. W. Liu, and S. He, "Onerestore: A universal restoration framework for composite degradation," in *Eur. Conf. Comput. Vis.*, 2024, pp. 255–272.
- [112] R. Li, L.-F. Cheong, and R. T. Tan, "Heavy rain image restoration: Integrating physics model and conditional adversarial learning," in *IEEE Conf. Comput. Vis. Pattern Recog.*, 2019, pp. 1633–1642.
- [113] R. Li, R. T. Tan, and L.-F. Cheong, "All in one bad weather removal using architectural search," in *IEEE Conf. Comput. Vis. Pattern Recog.*, 2020, pp. 3175–3185.
- [114] W. Chen, Z. Huang, C. Tsai, H. Yang, J. Ding, and S. Kuo, "Learning multiple adverse weather removal via two-stage knowledge learning and multi-contrastive regularization: Toward a unified model," in *IEEE Conf. Comput. Vis. Pattern Recog.*, 2022, pp. 17 632–17 641.
- [115] Y. Zhu, T. Wang, X. Fu, X. Yang, X. Guo, J. Dai, Y. Qiao, and X. Hu, "Learning weather-general and weather-specific features for image restoration under multiple adverse weather conditions," in *IEEE Conf. Comput. Vis. Pattern Recog.*, 2023, pp. 21 747–21 758.
- [116] T. Ye, S. Chen, J. Bai, J. Shi, C. Xue, J. Jiang, J. Yin, E. Chen, and Y. Liu, "Adverse weather removal with codebook priors," in *Int. Conf. Comput. Vis.*, 2023, pp. 12 619–12 630.
- [117] Y. Ai, H. Huang, X. Zhou, J. Wang, and R. He, "Multimodal prompt perceiver: Empower adaptiveness, generalizability and fidelity for all-in-one image restoration," in *IEEE Conf. Comput. Vis. Pattern Recog.*, 2024, pp. 25 432–25 444.
- [118] S. Sun, W. Ren, X. Gao, R. Wang, and X. Cao, "Restoring images in adverse weather conditions via histogram transformer," in *Eur. Conf. Comput. Vis.*, vol. 15080, 2024, pp. 111–129.
- [119] Y. Song, Z. He, H. Qian, and X. Du, "Vision transformers for single image dehazing," *IEEE Trans. Image Process.*, vol. 32, pp. 1927–1941, 2023.
- [120] Y. Zhang, S. Zhou, and H. Li, "Depth information assisted collaborative mutual promotion network for single image dehazing," in *IEEE Conf. Comput. Vis. Pattern Recog.*, 2024, pp. 2846–2855.
- [121] X. Chen, J. Pan, and J. Dong, "Bidirectional multi-scale implicit neural representations for image deraining," in *IEEE Conf. Comput. Vis. Pattern Recog.*, 2024, pp. 25 627–25 636.
- [122] S. Chen, T. Ye, Y. Liu, E. Chen, J. Shi, and J. Zhou, "Snow-former: Scale-aware transformer via context interaction for single image desnowing," *CoRR*, vol. abs/2208.09703, 2022.
- [123] D. Zheng, X. Wu, S. Yang, J. Zhang, J. Hu, and W. Zheng, "Selective hourglass mapping for universal image restoration based on diffusion model," in *IEEE Conf. Comput. Vis. Pattern Recog.*, 2024, pp. 25 445–25 455.
- [124] R. Zhu, Z. Tu, J. Liu, A. C. Bovik, and Y. Fan, "Mwformer: Multi-weather image restoration using degradation-aware transformers," *IEEE Trans. Image Process.*, vol. 33, pp. 6790–6805, 2024.
- [125] H. Zhang and V. M. Patel, "Density-aware single image de-raining using a multi-stream dense network," in *IEEE Conf. Comput. Vis. Pattern Recog.*, 2018, pp. 695–704.
- [126] R. Yasarla and V. M. Patel, "Uncertainty guided multi-scale residual learning-using a cycle spinning cnn for single image de-raining," in *IEEE Conf. Comput. Vis. Pattern Recog.*, 2019, pp. 8405–8414.
- [127] W. Wei, D. Meng, Q. Zhao, Z. Xu, and Y. Wu, "Semi-supervised transfer learning for image rain removal," in *IEEE Conf. Comput. Vis. Pattern Recog.*, 2019, pp. 3877–3886.
- [128] H. Gao, X. Tao, X. Shen, and J. Jia, "Dynamic scene deblurring with parameter selective sharing and nested skip connections," in *IEEE Conf. Comput. Vis. Pattern Recog.*, 2019, pp. 3848–3856.
- [129] W. Ren, S. Liu, H. Zhang, J. Pan, X. Cao, and M.-H. Yang, "Single image dehazing via multi-scale convolutional neural networks," in *Eur. Conf. Comput. Vis.*, 2016, pp. 154–169.
- [130] B. Li, X. Peng, Z. Wang, J. Xu, and D. Feng, "Aod-net: All-in-one dehazing network," in *Int. Conf. Comput. Vis.*, 2017, pp. 4770–4778.
- [131] Y. Qu, Y. Chen, J. Huang, and Y. Xie, "Enhanced pix2pix dehazing network," in *IEEE Conf. Comput. Vis. Pattern Recog.*, 2019, pp. 8160–8168.
- [132] Y. Dong, Y. Liu, H. Zhang, S. Chen, and Y. Qiao, "Fd-gan: Generative adversarial networks with fusion-discriminator for single image dehazing," in *AAAI Conf. Artif. Intell.*, 2020, pp. 10 729–10 736.
- [133] W. Yang, W. Wang, H. Huang, S. Wang, and J. Liu, "Sparse gradient regularized deep retinex network for robust low-light image enhancement," *IEEE Trans. Image Process.*, vol. 30, pp. 2072–2086, 2021.
- [134] C. Wei, W. Wang, W. Yang, and J. Liu, "Deep retinex decomposition for low-light enhancement," in *Brit. Mach. Vis. Conf.*, 2018, p. 155.
- [135] K. Xu, X. Yang, B. Yin, and R. W. H. Lau, "Learning to restore low-light images via decomposition-and-enhancement," in *IEEE Conf. Comput. Vis. Pattern Recog.*, 2020, pp. 2278–2287.
- [136] W. Yang, S. Wang, Y. Fang, Y. Wang, and J. Liu, "From fidelity to perceptual quality: A semi-supervised approach for low-light image enhancement," in *IEEE Conf. Comput. Vis. Pattern Recog.*, 2020, pp. 3060–3069.
- [137] Y. Zhang, X. Guo, J. Ma, W. Liu, and J. Zhang, "Beyond brightening low-light images," *Int. J. Comput. Vis.*, vol. 129, no. 4, pp. 1013–1037, 2021.
- [138] S. W. Zamir, A. Arora, S. H. Khan, M. Hayat, F. S. Khan, M. Yang, and L. Shao, "Learning enriched features for real image restoration and enhancement," in *Eur. Conf. Comput. Vis.*, vol. 12370, 2020, pp. 492–511.
- [139] X. Xu, R. Wang, C. Fu, and J. Jia, "Snr-aware low-light image enhancement," in *IEEE Conf. Comput. Vis. Pattern Recog.*, 2022, pp. 17 693–17 703.
- [140] C. Wang, H. Wu, and Z. Jin, "Fourllie: Boosting low-light image enhancement by fourier frequency information," in *ACM Int. Conf. Multimedia*, 2023, pp. 7459–7469.
- [141] S. Zhou, C. Li, and C. C. Loy, "Lednet: Joint low-light enhancement and deblurring in the dark," in *Eur. Conf. Comput. Vis.*, 2022.
- [142] O. Kupyn, T. Martyniuk, J. Wu, and Z. Wang, "Deblurgan-v2: Deblurring (orders-of-magnitude) faster and better," in *Int. Conf. Comput. Vis.*, 2019, pp. 8877–8886.
- [143] S. Cho, S. Ji, J. Hong, S. Jung, and S. Ko, "Rethinking coarse-to-fine approach in single image deblurring," in *Int. Conf. Comput. Vis.*, 2021, pp. 4621–4630.
- [144] S. Zhou, C. Li, and C. C. Loy, "Lednet: Joint low-light enhancement and deblurring in the dark," in *Eur. Conf. Comput. Vis.*, vol. 13666, 2022, pp. 573–589.

- [145] R. Li, H. Chen, F. Feng, Z. Ma, X. Wang, and E. Hovy, “Dual graph convolutional networks for aspect-based sentiment analysis,” in *Annu. Meeting Assoc. Comput. Linguist.*, 2021, pp. 6319–6329.
- [146] Z. Huang and L. Van Gool, “A riemannian network for spd matrix learning,” in *AAAI Conf. Artif. Intell.*, 2017.
- [147] J. Gu and C. Dong, “Interpreting super-resolution networks with local attribution maps,” in *IEEE Conf. Comput. Vis. Pattern Recog.*, 2021, pp. 9199–9208.



**Gang Wu** received the B.E. degree in the School of Computer Science and Technology from Soochow University, Jiangsu, China, in 2020. He is currently pursuing the Ph.D. degree in Faculty of Computing at Harbin Institute of Technology. His research interests include image restoration, representation learning, and self-supervised learning.



**Junjun Jiang** received the B.S. degree in Mathematics from the Huaqiao University, Quanzhou, China, in 2009, and the Ph.D. degree in Computer Science from the Wuhan University, Wuhan, China, in 2014.

From 2015 to 2018, he was an Associate Professor with the School of Computer Science, China University of Geosciences, Wuhan. From 2016 to 2018, he was a Project Researcher with the National Institute of Informatics (NII), Tokyo, Japan. He is currently a Professor with the School of Computer Science and Technology, Harbin Institute of Technology, Harbin,

China. His research interests include image processing and computer vision.



**Kui Jiang** received the M.E. and Ph.D. degrees from the School of Computer Science, Wuhan University, Wuhan, China, in 2019 and 2022, respectively. Before July 2023, he was a Research Scientist with the Cloud BU, Huawei. He is currently an Associate Professor with the School of Computer Science and Technology, Harbin Institute of Technology. He received the 2022 ACM Wuhan Doctoral Dissertation Award. His research interests include image/video processing and computer vision.



**Xianming Liu** received the B.S., M.S., and Ph.D. degrees in computer science from the Harbin Institute of Technology (HIT), Harbin, China, in 2006, 2008, and 2012, respectively. In 2011, he spent half a year at the Department of Electrical and Computer Engineering, McMaster University, Canada, as a Visiting Student, where he was a Post-Doctoral Fellow from 2012 to 2013. He was a Project Researcher with the National Institute of Informatics (NII), Tokyo, Japan, from 2014 to 2017. He is currently a Professor with the School of Computer Science and

Technology, HIT. His research interests include trustworthy AI, 3D signal processing and biomedical signal processing.



**Liqiang Nie** received the B.Eng. and Ph.D. degree from Xi'an Jiaotong University and National University of Singapore (NUS), respectively. After Ph.D., he continued his research in NUS as a research fellow for three years. He is currently the dean of the Department of Computer Science and Technology, Harbin Institute of Technology (Shenzhen). His research interests lie primarily in multimedia computing and information retrieval. He is an AE of IEEE TIP, IEEE TKDE, IEEE TMM, IEEE TCSVT, ACM ToMM, and Information Science. Meanwhile,

he serves as the chair of ICMR 2025, ICME 2025, and ACM MM 2027. He is a member of ICME steering committee. He has received many awards over the past four years, like SIGMM rising star in 2020, MIT TR35 China 2020, SIGIR best student paper in 2021, IEEE AI's 10 to Watch in 2022, ACM MM Best paper award in 2022, and the National Youth Science and Technology Award in 2024.